



저작자표시-비영리-변경금지 2.0 대한민국

이용자는 아래의 조건을 따르는 경우에 한하여 자유롭게

- 이 저작물을 복제, 배포, 전송, 전시, 공연 및 방송할 수 있습니다.

다음과 같은 조건을 따라야 합니다:



저작자표시. 귀하는 원저작자를 표시하여야 합니다.



비영리. 귀하는 이 저작물을 영리 목적으로 이용할 수 없습니다.



변경금지. 귀하는 이 저작물을 개작, 변형 또는 가공할 수 없습니다.

- 귀하는, 이 저작물의 재이용이나 배포의 경우, 이 저작물에 적용된 이용허락조건을 명확하게 나타내어야 합니다.
- 저작권자로부터 별도의 허가를 받으면 이러한 조건들은 적용되지 않습니다.

저작권법에 따른 이용자의 권리는 위의 내용에 의하여 영향을 받지 않습니다.

이것은 [이용허락규약\(Legal Code\)](#)을 이해하기 쉽게 요약한 것입니다.

[Disclaimer](#)

Master's Thesis

Porous Carbon Microparticles from
Phenylenediamine-Mellitic Acid Resin
for Energy Storage Devices

Byeongho Park

Department of Energy Engineering
Graduate School of UNIST

2016

Porous Carbon Microparticles
from Phenylenediamine-Mellitic Acid Resin
for Energy Storage Devices

Byeongho Park

Department of Energy Engineering
Graduate School of UNIST

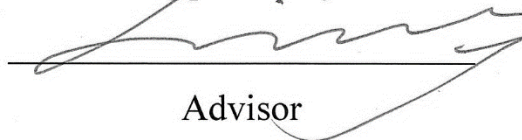
Porous Carbon Microparticles
from Phenylenediamine-Mellitic Acid Resin
for Energy Storage Devices

A thesis/dissertation
submitted to the Graduate School of UNIST
in partial fulfillment of the
requirements for the degree of
Master of Science

Byeongho Park

1. 15. 2016 Month/Day/Year of submission

Approved by



Advisor

Byeong-Su Kim

Porous Carbon Microparticles
from Phenylenediamine-Mellitic Acid Resin
for Energy Storage Devices

Byeongho Park

This certifies that the thesis/dissertation of Byeongho Park is
approved.

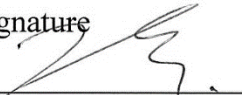
1. 15. 2016 Month/Day/Year of submission

signature



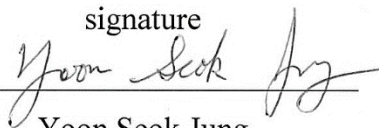
Advisor: Byeong-Su Kim

signature



Tae-Hyuk Kwon

signature



Yoon Seok Jung

Abstract

In part 1, porous carbon has been prepared in diverse synthetic methods and utilized for energy storage devices. We present carbon sphere (CS), a type of porous carbon, by carbonization of phenylenediamine-mellitic acid (PDA-MA) resin at high temperature annealing process. Sphere-shape PDA-MA resin is readily synthesized with the mixture of m-PDA and mellitic acid through hydrothermal condensation without additional reagents. We found that the CS from the resin has high porosity ($575 \text{ m}^2/\text{g}$) and a substantial nitrogen content ($\sim 7\%$). The CS was tested for anode of Li-ion battery and showed cycle retention of 274 mAh/g after 400 cycles. In addition, rate capability test of the CS revealed fast kinetics and 82% capability retention from 2C to 10C. Showing a chance for further improvement on coulombic efficiency by higher temperature carbonization, this research gave possibility for the CS in energy storage application.

In part 2, the performance of fiber-reinforced composites is governed not only by the nature of each individual component comprising the composite, but also by the interfacial properties between the fiber and the matrix. We present a novel layer-by-layer (LbL) assembly for the surface modification of glass fiber to enhance the interfacial properties between the glass fiber and epoxy matrix. Solution-processable graphene oxide (GO) and an aramid nanofiber (ANF) were employed as active components for the LbL assembly onto the glass fiber owing to their abundant functional groups and mechanical properties. We found that the interfacial properties of the glass fibers uniformly coated with GO and ANF multilayers, such as surface free energy and interfacial shear strength, were improved by 23.6% and 39.2%, respectively, compared with those of the bare glass fiber. In addition, the interfacial adhesion interactions between the glass fiber and epoxy matrix were highly tunable simply by changing the composition and the architecture of layers, taking the advantages of versatility of the LbL assembly.

Contents

PART 1. Porous Carbon Microparticles from Phenylenediamine- Mellitic Acid Resin for Energy Storage Devices

I. Introduction.....	1
1.1. Synthesis of CS.....	1
1.1.1. Hard templating synthesis	1
1.1.2. Soft templating synthesis.....	3
1.1.3. Hydrothermal condensation synthesis	4
1.1.4. Microemulsion polymerization synthesis	4
1.1.5. Extension of the Stöber method	5
1.2. Application	5
1.2.1. N, F-doped CS for supercapacitor	5
1.2.2. N-doped hierarchically porous CS for oxygen reduction reaction catalyst	7
1.2.3. Ultrahigh-surface-area hollow carbon sphere for energy storage.....	7
II. Experimental method & materials.....	7
2.1. Synthesis of phenylenediamine-mellitic acid (PDA-MA) resin	9
2.2. Synthesis of carbon sphere (CS).....	9
2.3. Characterizations	9
2.4. Cell fabrication and measurements for Li-ion battery	9
III. Results & discussion	10
3.1. Synthesis of N-doped CS from PDA-MA resin	10
3.2. Electrochemical performance of N-doped CS as an anode material for Li-ion battery	13
IV. Conclusion	16

PART 2. Highly Tunable Interfacial Adhesion of Glass Fiber by Hybrid Multilayers of Graphene Oxide and Aramid Nanofiber

I. Introduction.....	18
II. Experimental method & materials.....	20
2.1. Synthesis of positively charged graphene oxide (GO)	20
2.2 Synthesis of aramid nanofiber (ANF).....	20
2.3. Surface modification of glass fibers by LbL assembly.....	21

2.4. Sample preparation for microbond test.....	21
2.5. Characterizations	21
III. Results & discussion	22
IV. Conclusion	32

List of figures

PART 1

Figure 1. Schematic of the synthesis strategies of carbon sphere (CS). (a) Templating methods: HT process (i); ST process (ii, iii). (b) HT process for preparation of h-NCS. (c) HTC method. (d) Microemulsion polymerization method. (e) Extension of the Stöber method: direct polymerization (i); polymerization with silica nanoparticles (ii). Figure reproduced with permission from ref. 1, Nature Publishing Group..

Figure 2. Recent researches for the applications of energy conversion and storage. Figure reproduced from: ref. 36, ref. 5, and ref. 26, Creative Commons CC-BY, Nature Publishing Group.

Figure 3. Schematic of synthesis of carbon sphere (CS) from phenylenediamine-mellitic acid (PDA-MA) resin.

Figure 4. (a) *o*-PDA-MA, (c) *m*-PDA-MA, and (e) *p*-PDA-MA resin synthesized by ethanol solvothermal reaction. (b) *o*-PDA-MA, (d) *m*-PDA-MA, and (f) *p*-PDA-MA resin synthesized by hydrothermal reaction.

Figure 5. (a) SEM image of CS/700Ar. (b) XPS diffraction pattern of Resin and CS/700Ar. (c) Raman spectra of CS/700Ar and CS/700H₂. (d) XPS survey spectra, (e) carbon contents, and (f) nitrogen contents of Resin, CS/700Ar, CS/700H₂, CS/900Ar, and CS/900H₂.

Figure 6. Initial galvanostatic profile charge/discharge curves at 0.2 C (a–b), cycling performances (c–d), and rate capabilities (e–f) of CS/700Ar, CS/700H₂, CS/700H₂/CC, CS/900Ar/CC, and CS/900H₂/CC.

PART 2

Figure 1. Schematic of the preparation of a positively charged graphene oxide (GO) and negatively charged aramid nanofiber (ANF) multilayer coating on a glass fiber via nanoscale blending layer-by-layer (LbL) assembly.

Figure 2. (a) AFM image and height profile of graphene oxide (GO) and (b) TEM images of the aramid nanofiber (ANF) derived from Kevlar threads. The inset in part b shows the suspension of the ANF in dimethyl sulfoxide.

Figure 3. UV/vis spectra of GO/ANF multilayer films as a function of the number of bilayers. The inset indicates the absorbance at 330 nm depending on the number of bilayers.

Figure 4. SEM images of multilayer-coated glass fibers of (a) GO₁₀, (b) ANF₁₀, (c) (GO/ANF)₁₀, and (d) ANF₅/GO₅. The inset shows an enlarged view of each glass fiber. The scale bars are 20 μm (4 μm in the insets).

Figure 5. Surface free energy of the multilayer-coated glass fibers with different assembly and their corresponding schematics representing the glass fiber (sky-blue), GO layer (gray), and ANF layer (orange).

Figure 6. (a) Schematic of the microbond test for interfacial shear strength (IFSS). Epoxy resin is held in place with knives and measurement is carried out by pulling out a glass fiber. (b) Optical microscope image of the micro-droplet of epoxy resin on the glass fiber. (c) Pull-out force distribution depending on the immersion area within the epoxy matrix, and (d) Derived IFSS of the multilayer-coated glass fibers.

List of tables

PART 1

Table 1. Elemental analysis result of m-PDA-MA resin (Resin) and carbon sphere (CS) samples.

PART 2

Table 1. Configuration of the multilayer-coated glass fibers.

Table 2. Measured surface free energy (SFE) and interfacial shear strength (IFSS).

PART 1. Porous Carbon Microparticles from Phenylenediamine- Mellitic Acid Resin for Energy Storage Devices

I. Introduction

Carbon sphere (CS) has advantages of porous carbon materials with spherical shape, giving them attractive characteristics of tunable porosity, low particle size distribution, and regular geometry.¹ These novel materials are promising for catalysis, adsorption, water purifications, and energy storage application. Great efforts have been devoted to synthesis and application of porous CS. The researches of past ten years have allowed the synthesis of highly monodisperse CS, tunable size and type of pores, high specific surface area, and controllable surface properties.

Several synthetic strategies have been explored to design CS, such as hard and soft templating, hydrothermal condensation, microemulsion polymerization, and the Stöber method. With these efforts, various types of CS have been prepared with diameters ranging from nanometers to micrometers, as well as diverse pore types of micropore, mesopores, and macropores. Furthermore, CS can be functionalized by precursor design and post-functionalization, such as heteroatom doping and heat treatment. This dissertation summarizes major synthesis strategies for CS and applications especially for energy conversion and storage, including supercapacitors, oxygen reduction reaction catalysts, and Li-based secondary batteries.

1.1. Synthesis of CS

Various methods have been reported to prepare CS, such as hard templating, soft templating, hydrothermal, microemulsion polymerization, Stöber method, and heteroatoms-incorporated synthesis (Figure. 1). These methods enable versatile design to prepare desired types of CS, in contrast with other methods such as direct carbonization of hydrocarbons and chemical vapor deposition.^{2,3} According to the design, CS can be classified as solid CS (s-CS), hollow CS (h-CS), core-shell CS (cs-CS) and yolk-shell CS (ys-CS). The CS also can be classified by pore size, giving microporous CS (micro-CS), mesoporous CS (meso-CS), micro-mesoporous CS and macroporous CS. The molecular-level synthetic strategies result in CS with adjustable properties and are thus more attractive in experimental aspects. The further optimization of both structure and functionality is expected to discover CS with desired characteristics for applications of energy conversion and storage.

1.1.1. Hard templating synthesis

The most straightforward synthetic way of meso-CS and h-CS is taking advantage of well-defined silica templates. Meso-CS can be prepared by nanocasting strategy, which impregnates mesoporous silica sphere hard template (HT) with carbon precursors. Mesoporous silica spheres are obtained by

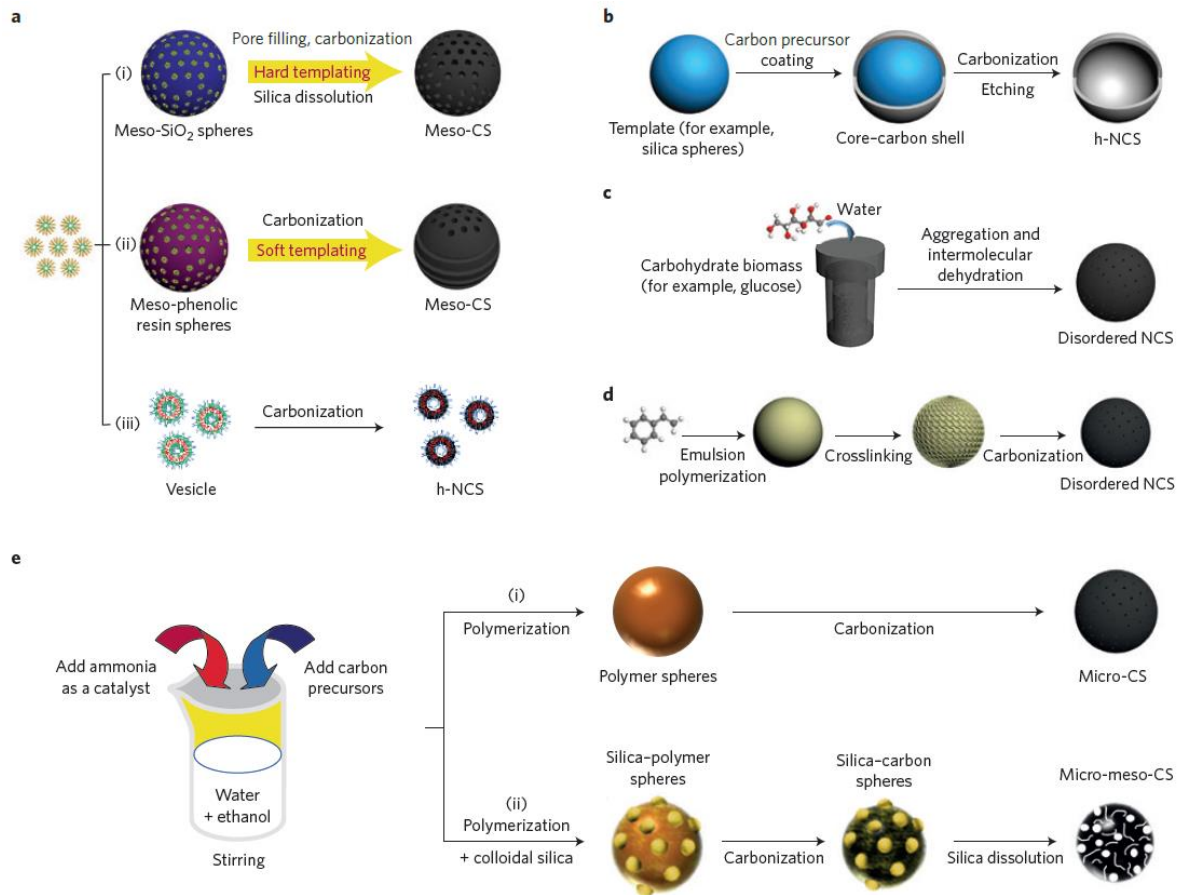


Figure 1. Schematic of the synthesis strategies of carbon sphere (CS). (a) Templating methods: HT process (i); ST process (ii, iii). (b) HT process for preparation of h-NCS. (c) HTC method. (d) Microemulsion polymerization method. (e) Extension of the Stöber method: direct polymerization (i); polymerization with silica nanoparticles (ii). Figure reproduced with permission from ref. 1, Nature Publishing Group.

facile sol-gel preparation with silica precursors and surfactants. After filling their pores with carbon precursors, meso-CS is made by subsequent pyrolysis of the silica-carbon composite, followed by removal of the silica template with HF or NaOH etchants solution. A. Stein and co-workers reported the synthesis of meso-CS with mesoporous silica HT method for the first time.⁴ The size and type of meso-CS are finely tuned by controlling the properties of mesoporous silica templates.

Through the nanocasting of mesoporous silica, it is demonstrated to synthesize mesoporous carbon structures by embedding solid silica nanoparticles.⁵ Impregnation of carbon precursor into confined template of inverse opal structure and removal of the template is also tried as well.⁶

HT method is also regarded as a concise way to synthesize h-CS. First, sphere-shaped hard templates that are readily removable are prepared, and carbon precursors are coated on the templates. After the preparation, the templates are removed to obtain h-CS. Polystyrene and silica are considered as appropriate hard templates for the synthesis of h-CS. As carbon precursors, glucose,⁷ dopamine,⁸ resorcinol-formaldehyde resin,⁹⁻¹³ and polyanilines¹⁴ have been studied to prepare h-CS.

Hard templating is the facile method that obtains negative replicas of silica templates or other types of hard templates. However, the inconvenient preparation of hard templates and dangerous etchant for the removal of templates, such as HF and NaOH, are the drawbacks of the HT method. Although hard templates of well-controlled properties enable the direct control of particle size, pore type, and morphology, the hazardous chemicals and tedious preparation process of hard templates limit extensive applications of HT method.

1.1.2. Soft templating synthesis

Soft templating (ST) method does not need to prepare and remove hard templates. In the contrast with the HT method, the way for direct fabrication of meso-CS has been studied by employing soft templates such as self-assembled micelles of amphiphilic block copolymers or surfactants.¹⁵⁻¹⁹ The ST method involves carbonization of self-assembled soft templates and carbon precursors, which make mesopore and carbon framework respectively. Since soft templates are self-assembled during the preparation, additional processes are not required for template fabrication. The soft templates, such as polymeric vesicles containing volatile solvent, are automatically decompose during carbonization, therefore no additional processes for the removal of soft templates are accompanied.¹⁷⁻²² The ST method also has drawbacks. Soft templates that are made of organic molecules exhibit week stability of self-assembly structure and aggregation of adjacent templates by crosslinking during CS formation.

In recent researche, types of meso-CS were fabricated by employing PS-*b*-PEO (poly(styrene)-block-poly(ethylene oxide)) block copolymer as soft template, and the pore size of the meso-CS was adjustable by controlling the molecular weight of PS and PS part of the block copolymer.²³ Spray-drying pyrolysis was also studied to enhance the yield of CS.^{24,25} By generating aerosol with precursor solution containing block copolymers and heating, meso-CS has been successfully prepared via

aerosol-assisted self-assembly for the large scale. The ST method is used to fabricate h-CS as well. It has been reported that non-ionic copolymer surfactants such as Triton X-100 or Pluronic F127 were used and various kinds of h-CS were prepared by relatively simple processes.^{26,27}

In general, the ST method is simple and broadly applicable for the synthesis of diverse types of CS including meso- and h-CS, as well as more complex CS.²¹ Despite of the challenges such as low yield, week structural stability of the templates, broad particle size distribution, various studies are proceeding to overcome the drawbacks.

1.1.3. Hydrothermal condensation synthesis

The hydrothermal condensation (HTC) method consists of dehydration, condensation, polymerization, and carbonization of carbon precursors. The condensation by dehydration of carbon precursors that possess hydroxyl groups forms sphere-shape agglomerates ranging from 200 nm to 5 μm diameter. The HTC method has been spotlighted owing to the possibility that CS can be synthesized from biomass precursors, including glucose, fructose, and cyclodextrin.^{28–30}

For the condensation in high temperature (160 – 200 $^{\circ}\text{C}$) aqueous solution, high pressure container is used. The HTC method is a feasible way to synthesize CS without additional templates by condensation reaction of precursors, and the CS fabricated by the HTC method has disordered micropore structure. However, broad applications with various carbon precursors are still restricted due to the difficulties of tuning pore structure and size of CS. The facing challenges are facile control for preparing well-defined structure and size of CS, such as meso-CS. Comprehensive understanding concerning to the complex chemistry in the HTC method and discovery of the suitable carbon precursors that enable to form well-defined structure are required.

1.1.4. Microemulsion polymerization synthesis

The microemulsion polymerization method is another synthesis strategy that does not involve templates for CS fabrication. The strategy have been the most popular for the preparation of monodisperse polymeric spheres such as polystyrene (PS) and poly(methyl methacrylate) (PMMA) beads. It was tried to prepare CS by pyrolysis of the polymeric spheres, but the attempts failed to convert the monodisperse polymeric spheres to carbonized structures because of low thermal stability and severe agglomeration of the spheres.^{31,32} As a solution, the polymeric sphere were internally crosslinked to improve the structural stability during carbonization. By introduction of divinylbenzene crosslinker along with styrene monomer, micro-CS was obtained after crosslinking and pyrolysis.³³ The same strategy can be used to synthesize h-CS, by adjusting the degree of post-crosslinking reaction and removing un-crosslinked core. The microemulsion method uses emulsion state to form sphere shape of CS without templates, therefore versatile synthesis is possible by controlling emulsion state. However, major drawbacks are agglomeration between the templates and low yield of CS.

1.1.5. Extension of the Stöber method

The Stöber synthesis is the reaction for general synthesis of monodisperse silica spheres. In 2011, G. Q. Lu and coworkers achieved the application of the Stöber method to synthesize CS,³⁴ by understanding that sol-gel reaction of silica sphere is applicable to resorcinol-formaldehyde reaction for polymeric spheres formation. After pyrolysis, it was demonstrated that the micro-CS whose average diameter is ranging from 150–900 nm is successfully synthesized with high yield. Other derivatives of resorcinol, including 3-methylphenol, 1,3,5-trihydroxybenzene, isomers of aminophenol have been employed to synthesize monodisperse CS.³⁵ By selecting proper precursors and combining with other methods, many kinds of CS with various structures, such as core-shell and yolk-shell, were fabricated via the Stöber method.^{9,13}

The Stöber method that is expanded to the synthesis of diverse CS structures has provided genuine opportunities by combining with other synthetic strategy such as hard templating. In addition, the Stöber method exhibits relatively high yield, inexpensive cost, facile scale-up, and tremendous chances for molecular-level design of functionalized CS. The disadvantage of the Stöber methods is the limited choice of precursors, but efforts to find out the proper reagents for the Stöber method are ongoing in various ways.

1.2. Application

I briefly summarize a few recent examples of the applications especially for energy conversion and storage (Figure 2). Synthetic methods such as hard and soft templating have been used for the preparation of monodisperse CS with tunable particle size and various functionalities. With diverse types of CS, a number of applications were tried, including supercapacitors, oxygen reduction reaction catalysts, and Li-ion batteries. The CS was functionalized for the use of the applications, such as nitrogen, fluorine co-doped CS for supercapacitors, nitrogen-doped hierarchically porous with both of micro- and mesopore for ORR, and hollow CS for Li-S batteries electrode materials.

1.2.1. N, F-doped CS for supercapacitor

Various porous nanostructures with large surface area have been utilized for electrical double-layer capacitors. However, the porous materials usually have low mass density, therefore they showed poor volumetric capacitance. F. Gao and coworkers fabricated N,F-doped CS for supercapacitor,³⁶ by doping fluorine and nitrogen into CS by exposing fluorine and nitrogen source gas at high temperature. Comparing to the conventional carbon materials showing poor volumetric capacitance below 250 F/cm³, the N, F-doped CS with micropore has exceptional capacitance of 521 F/cm³. The N,F-doped CS also exhibited excellent cyclic stability showing no loss of capacitance during 10,000 cycles in both acid and base electrolytes at 5 A/g current density.

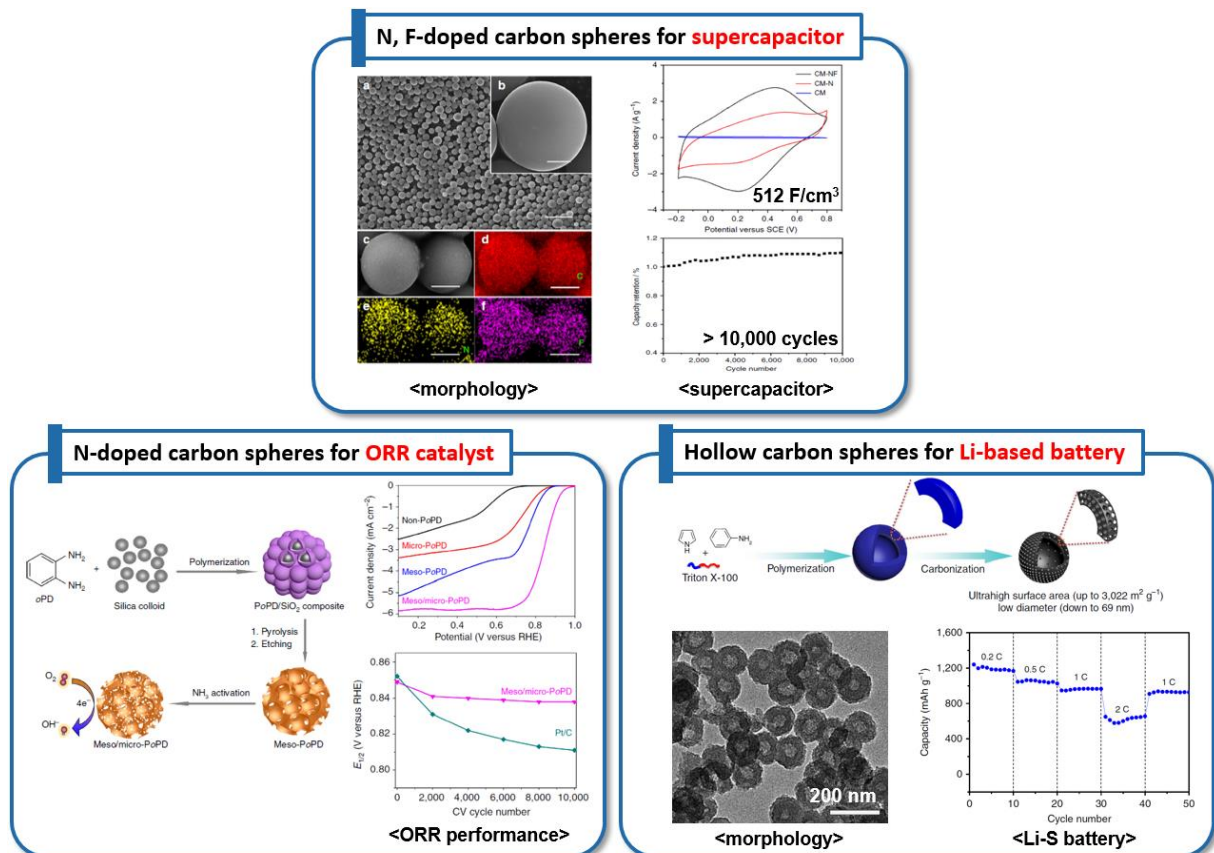


Figure 2. Recent researches for the applications of energy conversion and storage. Figure reproduced from: ref. 36, ref. 5, and ref. 26, Creative Commons CC-BY, Nature Publishing Group.

1.2.2. N-doped hierarchically porous CS for oxygen reduction reaction catalyst

Many researches have tried to substitute conventional platinum-based oxygen reduction reaction (ORR) catalysts for fuel cells due to its poor durability and expensive price. As inexpensive, durable alternatives of platinum-based catalysts, porous carbon materials are considered as promising candidates of metal-free electrocatalyst for ORR reaction due to their unique electronic properties.

K. Müllen and coworkers prepared hierarchically micro-, mesoporous CS with nitrogen doping and tested them for ORR catalysts.⁵ Porous CS with micro-, mesopore was synthesized by using silica nanoparticles as a template and activating CS by ammonia. Templating and removing silica nanoparticles introduced mesopore into CS, and ammonia activation introduced micropore. The electrochemical performance of N-doped CS with 1280 m²/g of specific surface area was compared with that of a platinum-based electrocatalyst. When Zn-air batteries were fabricated with the CS as ORR catalysts, the CS catalysts showed better performance compared to state-of-the-art Pt/C catalyst.

1.2.3. Ultrahigh-surface-area hollow carbon spheres for energy storage

Hollow carbon spheres are attractive porous carbon material with the unique characteristics of low density, and large interior void space. D. Wu and coworkers synthesized ultrahigh-surface-area hollow CS without hard templates such as silica spheres, by using triton X-100 micelle as a soft template.²⁶ After carbonization of pyrrole and aniline comonomer along with the micelle, h-CS with 3,022 m²/g of specific surface area was synthesized.

The nitrogen-doped ultrahigh-surface-area h-CS was utilized for various applications, such as organic vapor adsorption, supercapacitor, and electrode materials of Li-S battery. Excellent adsorption properties were shown and the supercapacitor with hollow CS performed very well. In addition for the Li-S application, the hollow CS was successfully impregnated sulphur by melt-diffusion method, and the hollow CS showed high capacitance as cathode host materials of Li-S batteries.

Among the numerous synthetic methods and applications of CS, here we report porous CS from phenylenediamine-mellitic acid (PDA-MA) resin for anode materials of secondary Li-ion batteries as energy storage application (Figure 3). The prepared CS from PDA-MA resin possesses a specific surface area of 575 m²/g, spherical shape with diameters about 1–2 μm, and substantial contents of nitrogen doping. With these nitrogen-doped porous CS, anodes for Li-ion batteries were fabricated. The best specific capacity of the anodes is 274 mA/g after 400 cycles at rate of 1 C. Considering that further optimization of the size of CS and specific surface area is in progress, the CS made from PDA-MA resin is expected to present utilitarian value for energy storage applications.

II. Experimental method & materials

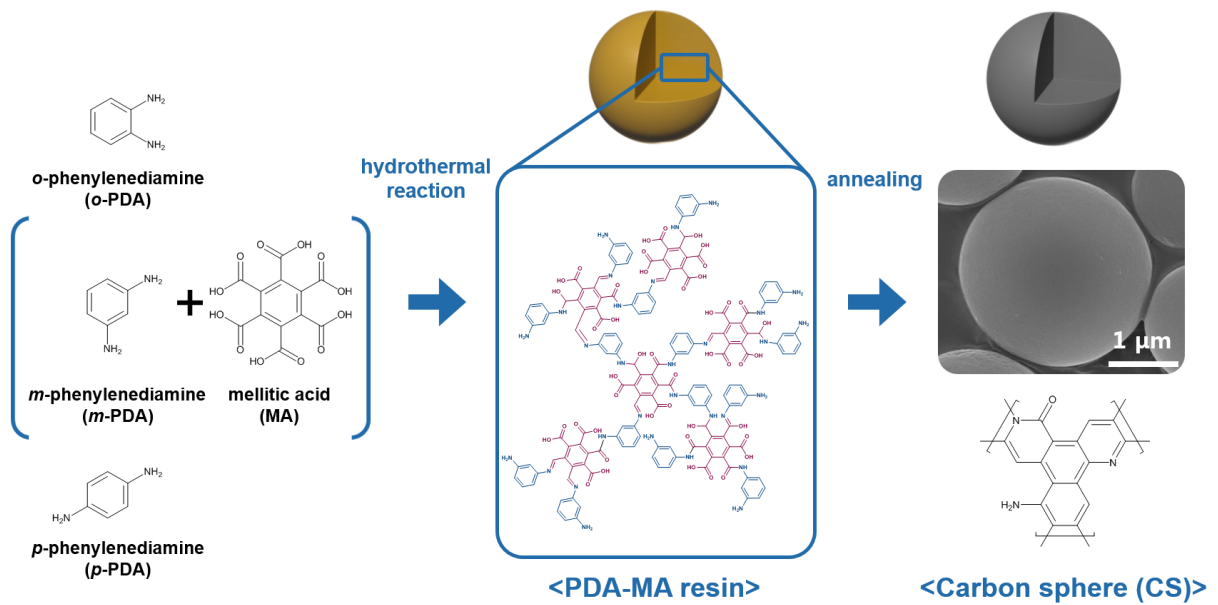


Figure 3. Schematic of synthesis of carbon sphere (CS) from phenylenediamine-mellitic acid (PDA-MA) resin.

2.1. Synthesis of phenylenediamine-mellitic acid (PDA-MA) resin

The synthesis of the PDA-MA resin involves hydrothermal reaction of three isomers of PDA and MA (Tokyo Chemical Industry Co.) in water or ethanol as solvents. Specifically, 0.5 wt% mixture solution of PDA and MA solution was prepared in 3:1 ratio. PDA-MA resin was synthesized by hydrothermal reaction of the solution for 12 hours at 180 °C. After the hydrothermal reaction, the precipitate was separated by centrifugation and were washed with water several times by repeating centrifugation.

2.2. Synthesis of carbon spheres (CS)

The CS was prepared by carbonization of the PDA-MA resin. Among the PDA-MA resin samples, spherically shaped resin, synthesized from *m*-PDA and MA in hydrothermal reaction, was thermally treated for two hours for carbonization. CS/700Ar and CS/900Ar samples were obtained by thermal treatment with argon gas flow (100 sccm) at 700 °C and 900 °C, respectively. Likewise, CS/700H₂ and CS/900H₂ samples were obtained by thermal treatment with the flow of 4% hydrogen in argon carrier gas (100 sccm) at 700 °C and 900 °C, respectively. Carbon coating of CS was carried out by flow of acetylene gas (500 sccm) at the same temperature with the carbonization of PDA-MA resin for 10 minutes.

2.3. Characterizations

Scanning electron microscope (SEM) was performed using a S-4800 (Hitach) with accelerating voltage of 10 kV. X-ray diffraction (XRD) experiment was carried out by D8 ADVANCE (Bruker) with K α radiation of Cu as X-ray source. Raman spectroscopy was measured by alpha300R (WITec) with samples that are prepared on oxidized Si wafer. X-ray photoelectron (XPS) spectroscopy was performed using K-alpha (ThermoFisher). Elemental analysis (EA) was carried out on a Flash2000 (Thermo Scientific). Nitrogen adsorption/desorption isotherms were analyzed at 77 K with ASAP2420 (Micromeritics Instruments), and specific surface area was calculated by the Brunauer–Emmett–Teller (BET) method based on the isotherm graph.

2.4. Cell fabrication and measurements for Li-ion battery

The electrochemical performance was tested by using galvanostatic cycler with coin type cells (2016R type). The coin type cells were fabricated by employing Cu foil coated with CS samples as a working electrode, Li foil as counter electrode, which are half-cell. For the working electrodes, 80 wt% CS, 10 wt% conducting agent (Super P carbon black), and 10 wt% polymeric binder (polyvinylidene fluoride, PVDF) were dissolved in N-methyl-2-pyrrolidone (NMP). The paste of the mixture applied on Cu foil by doctor blade and dried at 150 °C vacuum. The electrolyte was composed of 1.3 M LiPF₆ in the mixture of ethylene carbonate/diethylcarbonate (EC/DEC, 3:7 vol%) with 10 wt% fluorinated

ethylene carbonate (FEC) additive. The coin cells were tested by galvanostatic charge/discharge at different scan rates between 3.0 V and 0.01 V (vs. Li/Li). Galvanostatic measurements were conducted by WBCS-3000 battery cycler (Wonatech Co.) at room temperature.

III. Results & discussion

3.1. Synthesis of N-doped CS from PDA-MA resin

A facile synthesis of N-doped CS, which includes phenylenediamine (PDA) and mellitic acid (MA) as precursors, was developed for energy storage applications. Nitrogen doping on carbon analogues that are composed of delocalized electron system improves electrochemical performance,³⁷ thus isomers of PDA that consist of phenyl and two amine groups were used with MA, which contain carboxylic acid groups. By the condensation reaction of amine group of PDA and carboxylic acid of MA, it is intended to synthesize CS with N-doped aromatic carbon structure without harsh heat treatment for graphitization.

By the combination of three isomers of PDA and MA in hydrothermal and ethanol solvothermal condensation, PDA-MA resin samples were prepared. Although the condensation reaction between amine groups of PDA and carboxylic acid groups of MA does not readily occurs without catalyst, it is reported that amide formation by the condensation of amine and carboxylic acid become favorable in hydrothermal and solvothermal condition.³⁸ The interesting aspect is the morphology of resulting PDA-MA resins which were totally different depending on the types of PDA and solvent (Figure 4). Uniform morphology was not observed in the case of *o*-PDA-MA and *p*-PDA-MA resins, while *m*-PDA-MA resins have micro-sized particles with regular shape. Especially, *m*-PDA-MA that underwent hydrothermal condensation exhibited sphere-shaped carbon structure. These distinctions between the resins result from directions of amine groups in the isomers of PDA. The difference in amine group orientations is considered to influence the formation of amide bond network of PDA-MA resin in terms of steric hindrance. In addition, difference in vapor pressure and reactivity between water and ethanol solvents also cause structural distinction of the PDA-MA resin. The spherical shape *m*-PDA-MA resin from hydrothermal condensation was denoted as Resin, and four types of CS were prepared after carbonization.

Depending on the temperature and atmosphere of carbonization, four CS samples were obtained. Elemental composition of the Resin and the four CS samples were analyzed (Table 1). After the carbonization, carbon contents was increased, while hydrogen and oxygen contents were reduced. This is because of the graphitization and reduction of functional groups of resin, such as carboxylic acid and amide group. Considerable nitrogen content was conserved about 7 at% for 700 °C annealing and expected to enhance electrochemical performance as an anode of Li-ion batteries. For CS/700Ar, the Brunauer–Emmett–Teller (BET) surface area was calculated to be 575 m²/g and the average pore size was 1.58 nm.

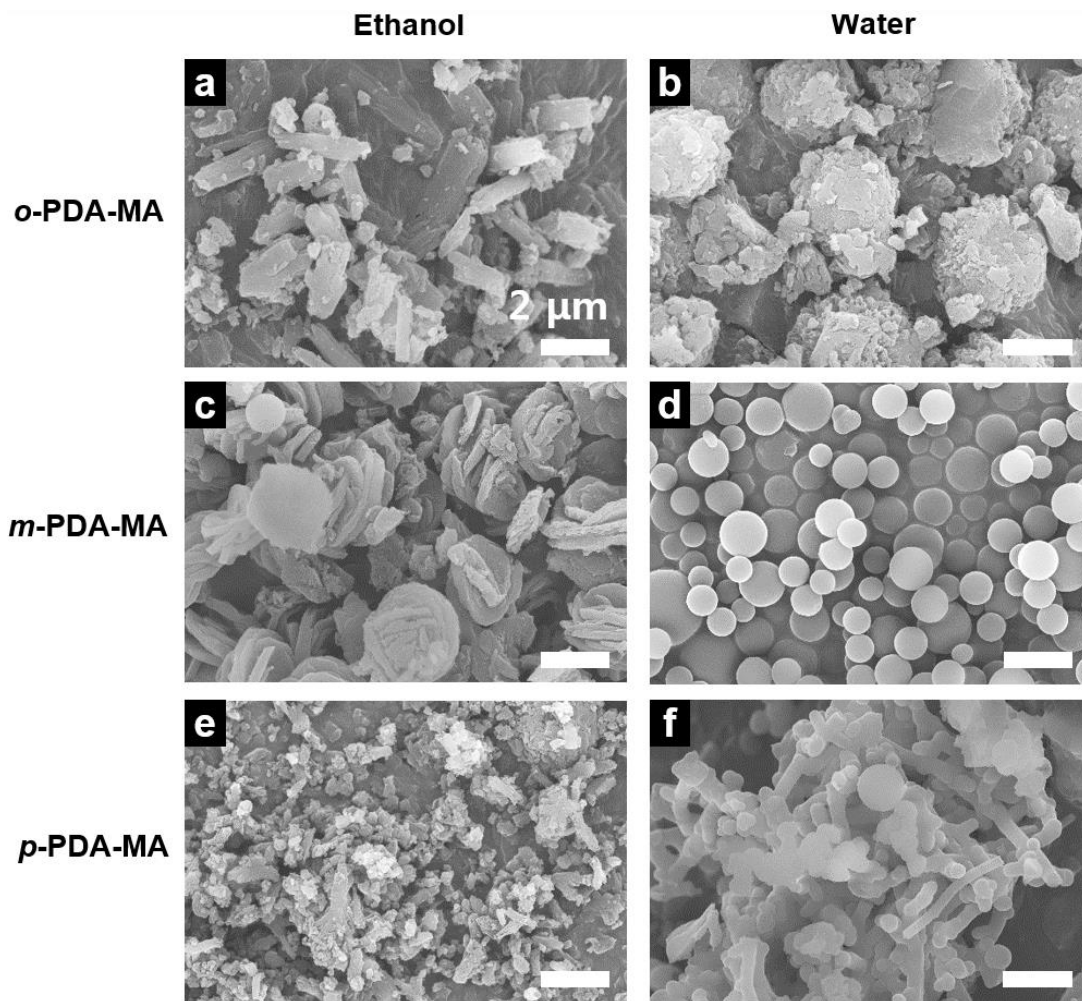


Figure 4. (a) *o*-PDA-MA, (c) *m*-PDA-MA, and (e) *p*-PDA-MA resin synthesized by ethanol solvothermal reaction. (b) *o*-PDA-MA, (d) *m*-PDA-MA, and (f) *p*-PDA-MA resin synthesized by hydrothermal reaction.

Table 1. Elemental analysis result of m-PDA-MA resin (Resin) and carbon spheres (CS) samples.

#	Preparation	Nomenclature	Carbon	Hydrogen	Nitrogen	Oxygen
1	<i>m</i> -PDA-MA resin	Resin	48.5%	28.5%	8.5%	14.5%
2	Resin after 700 °C Ar annealing	CS/700Ar	74.8%	13.9%	7.1%	4.2%
3	Resin after 700 °C H₂ annealing	CS/700H₂	71.2%	18.0%	6.8%	4.2%
4	Resin after 900 °C Ar annealing	CS/900Ar	82.2%	9.3%	5.0%	3.5%
5	Resin after 900 °C H₂ annealing	CS/900H₂	82.3%	10.3%	3.7%	3.7%

Structural features of CS/700Ar was measured (Figure 5a). The SEM image shows the morphology of CS after the carbonization displaying uniform spherical shape and diameter ranging from 1 to 2 μm . Porosity on the surface of the CS was not observed in the SEM image. X-ray diffraction (XRD) patterns of Resin and CS/700Ar show broaden diffraction peaks at 2θ around 22° and 44° , corresponding to (002) and (101) planes of graphite (Figure 5b). The broad and rather distinctive peaks from the background peak indicate dominant amorphous carbon structures of typical hard carbon. Raman spectra of CS/700Ar and CS/700H₂ show D-band located at 1,363 cm^{-1} and G-band located at 1,590 cm^{-1} , ascribed to the vibration peak of defective carbon and the vibration peak of sp^2 -bonded carbon, respectively (Figure 5c). The D to G ratios (I_D/I_G) of CS/700Ar and CS/700H₂ were 1.26 and 1.27, indicating considerably defective structure and the nature of nearly graphitizable hard carbon.

Chemical states of elements in Resin and CS were investigated by XPS (Figure 5d–5f), which revealed typical peaks for C1s, N1s, and O1s in the XPS survey spectra. High-resolution XPS spectra of C1s and N1s were further deconvoluted to analyze the bonding state of carbon and nitrogen. The peaks at 284.5, 285.3, 286.3, 287.2, 288.1, and 289.2 eV are attributed to sp^3 , sp^2 , C–O, C–N, C–N, C=O, and O–C=O configurations, respectively. The change of carbon contents indicates the degree of carbonization. After the carbonization of Resin, the carbon contents were increased from 48.5% to 74.8%, 71.2%, 82.2%, and 82.3% for Resin, CS/700Ar, CS/700H₂, CS/900Ar, and CS/900H₂, respectively. The hydrogen atmosphere during carbonization raises the ratio of sp^2 . The N1s spectra could be deconvoluted into four different peaks at 398.4, 399.7, 400.9, and 402.1 eV, which are attributed to the pyridinic-N, pyrrolic-N, graphitic-N, and protonated-N. Appearance of considerable graphitic-N contents, which is bonded to three carbon atoms within the graphene plane, indicates successful doping of nitrogen into the structure of CS.

3.2. Electrochemical performance of N-doped CS as an anode material for Li-ion battery

Electrochemical performance of CS depending on the condition of carbonization and carbon coating (CC) was measured. First, CS/700Ar, CS/700H₂, and CS/700H₂/CC which is carbon coated CS/700H₂ were compared in the first cycle discharge (lithiation)-charge (delithiation) curves. Reductive atmosphere of hydrogen gas and carbon coating was expected to improve coulombic efficiency by reducing functional groups and by increasing electric conductivity. The coulombic efficiency of CS/700Ar, CS/700H₂, and CS/700H₂/CC were 53.2%, 49.0%, and 62.8%, while they show initial discharge capacity of 978, 1004, and 680 mAh/g, respectively (Figure 6a). The irreversible capacity was reduced after carbon coating, decreasing from 458 mAh/g of CS/700Ar to 253 mAh/g of CS/700H₂/CC. This may be attributed to the increase of conductivity as expected above.

Cycling performance was measured for 100 cycles at 0.2 C-rate (Figure 6c). CS/700Ar, CS/700H₂, and CS/700H₂/CC showed the specific capacity of 233, 208, and 276 mAh/g, respectively. For the

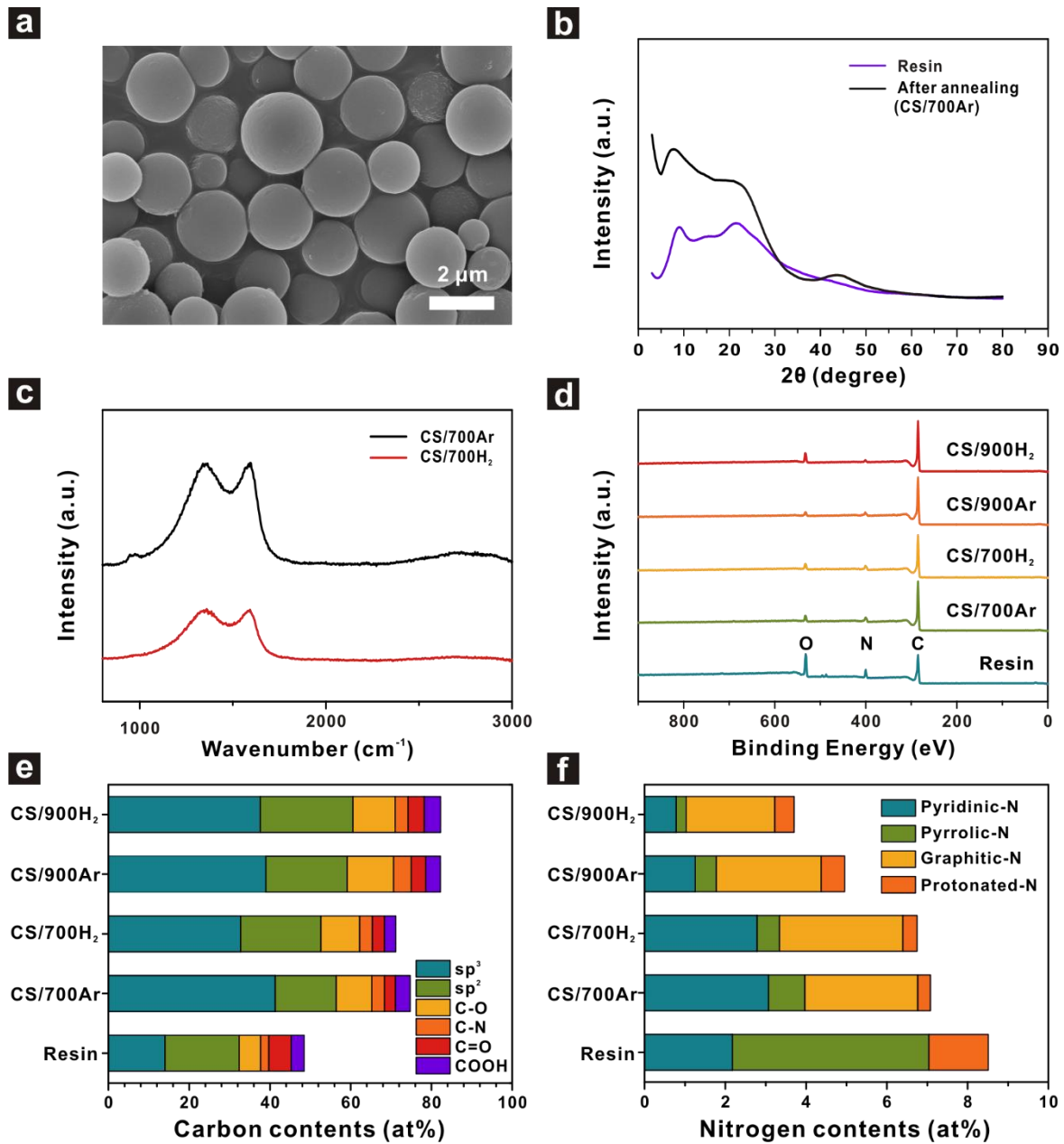


Figure 5. (a) SEM image of CS/700Ar. (b) XPS diffraction pattern of Resin and CS/700Ar. (c) Raman spectra of CS/700Ar and CS/700H₂. (d) XPS survey spectra, (e) carbon contents, and (f) nitrogen contents of Resin, CS/700Ar, CS/700H₂, CS/900Ar, and CS/900H₂.

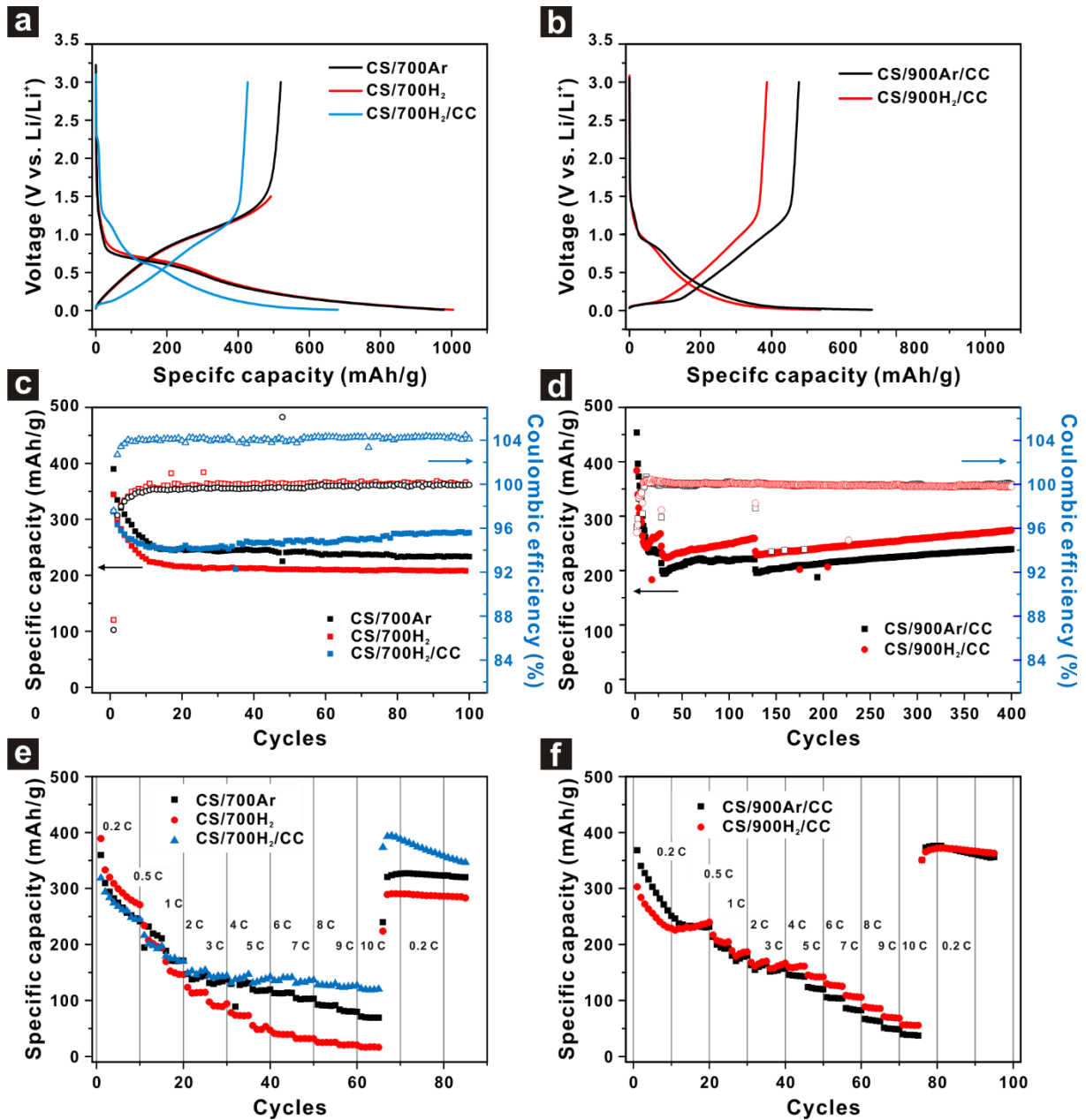


Figure 6. Initial galvanostatic profile charge/discharge curves at 0.2 C (a–b), cycling performances (c–d), and rate capabilities (e–f) of CS/700Ar, CS/700H₂, CS/700H₂/CC, CS/900Ar/CC, and CS/900H₂/CC.

first 10 cycles, the capacity rapidly degraded for all samples. The degradation results from irreversible reaction with residual functional groups or terminal hydrogen of CS. Interestingly, CS/700H₂/CC exhibited gradual increase of the specific capacity. The tendency suggests that slow activation of CS with more reaction sites.³⁷ Rate capability was investigated to measure capacity depending on the speed of discharge-charge. The superior performance of CS/700H₂/CC was also shown at high C-rate compared to the others. CS/700H₂/CC retained 82% of its capacity from 2 to 10 C-rate, while CS/700Ar and CS/700H₂ exhibited sharp decrease of capacity. The capacity retention at high C-rate can be explained by higher internal electronic conductivity of the carbon-coated active materials.

For the optimization of heat treatment process, higher carbonization temperature was attempted with carbon coating (Figure 6b). Decrease of irreversible reaction was expected by the rise of carbonization temperature. Furthermore, cycling capability test was carried out with gradual C-rate shift (Figure 6d), which is programmed with 3 cycles of 0.05 C, 5 cycles of 0.1 C, 20 cycles of 0.2 C, 100 cycles for 0.5 C, ended in 1 C-rate until 400 cycles. The gradual C-rate shift is conducted to overcome poor initial coulombic efficiency and slow activation of the CS. To highlight superior rate capability of CS as shown above, higher discharge-charge rate of 1 C was measured. It has been found that CS/900Ar/CC and CS/900H₂/CC showed the higher capacity than CS/700H₂/CC at 0.2 C-rate in rate capability test. After 400 cycles, the specific capacities were 208 and 274 mAh/g for CS/900Ar/CC and CS/900H₂/CC. In consideration of the condition of the higher C-rate for the two samples, CS with the higher carbonization temperature exhibited enhanced cycling performances. In contrast with CS/700H₂ that has lower capacity than CS/700Ar, the cyclic performance graph indicate enhanced capacity of CS/900H₂/CC than that of CS/900Ar/CC. The reduction of irreversible functional group of CS may require higher carbonization temperature. Nevertheless, the rate capability of CS/900Ar/CC and CS/900H₂/CC were deteriorated by the elevated carbonization temperature. The specific capacity of CS/700H₂/CC, CS/900Ar/CC, and CS/900H₂/CC were 120, 56, and 37 mAh/g at 10 C-rate. Compared to the specific capacity of CS/700H₂/CC at 10 C, that of CS/900Ar/CC and CS/900H₂/CC are dramatically decreased. This result partially correspond to decreased nitrogen contents of the two samples after 900 °C carbonization. The additional control experiment of carbonization temperature is required for the optimization of electrochemical performance.

IV. Conclusion

We demonstrate facile way to synthesize N-doped carbon spheres by carbonization of *m*-phenylenediamine-mellitic acid resin at high temperature. Sphere-shape PDA-MA resin is successfully synthesized from the mixture of *m*-PDA and mellitic acid through hydrothermal condensation without additional surfactants or templates. The synthesized carbon spheres have high porosity (575 m²/g) and remarkable nitrogen contents (~7%). The carbon spheres were tested for

anode of Li-ion battery and showed cycle retention of 274 mAh/g after 400 cycles at 1 C-rate. In addition, rate capability test of the CS revealed good electrochemical performance at high C-rate and show 82% capability retention from 2C to 10C. Suggesting a chance for the further improvement on electrochemical performance, this research gives possibility to the carbon spheres for energy storage application. The carbon spheres are expected to present utilitarian value for energy conversion and storage applications.

PART 2. Highly Tunable Interfacial Adhesion of Glass Fiber by Hybrid Multilayers of Graphene Oxide and Aramid Nanofiber

I. Introduction

Nanocomposites containing inorganic and organic fibers within a matrix of polymers are attracting significant scientific and industrial interest in various fields with high-performance applications, including construction, transportation, sports, and aerospace.³⁹⁻⁴¹ In general, the performance of fiber-reinforced composites is governed not only by the nature of each individual component, but also by the interfacial properties between the fiber and the matrix.⁴² For example, the effective load transfer from the matrix to the fillers is essential to reduce stress localization and thus improves the integrated mechanical properties.⁴³ Consequently, significant efforts have been made toward enhancing the interfacial adhesion between the matrix and fillers in the polymer composite, such as enhancing the chemical activity of the fillers or increasing the surface area by tailoring fiber/matrix interfaces.^{42,43}

Graphene, a monolayer of a two-dimensional aromatic carbon lattice, has recently emerged as a promising nanomaterial in various fields owing to its superior mechanical, thermal, and electrical properties.⁴⁴⁻⁴⁶ In particular, solution-processable graphene oxide (GO), typically prepared by chemical exfoliation processes from graphite, possesses unique advantages suitable for nanocomposites.⁴⁷ First, abundant surface functional groups provide GO with excellent dispersity and offer opportunities for further chemical modifications with matrix polymers for interfacial engineering. Second, the unique two-dimensional sheet-like geometry of GO together with its high surface area makes it highly effective at deflecting cracks at the interface of the fiber and matrix polymer. To date, there are many reports on the production of graphene containing polymer composites with improved static, fatigue, and electrical properties.^{45,48} The successful translation of the superior material properties of graphene to macro-scale composite properties often relies on the processing condition of the additive and the matrix. For example, melt blending, extrusion, post, or in situ polymerization methods are often employed to incorporate active graphene in the polymer matrix.⁴⁹⁻⁵²

Since the development of aramid in early 1960s, various types of aramid fiber, such as Kevlar[®], have been received considerable attention for the design of high performance materials, owing to their outstanding mechanical properties.⁵³ In particular, the ability to strengthen the matrix with high tensile strength has provided a remarkable reinforcement of composites.^{54,55} Recently, Kotov and co-workers reported a stable dispersion of aramid nanofiber (ANF) from Kevlar threads under a strong basic condition, in order to overcome the issues in limited solution processability.⁵⁶ The ANF with high aspect ratio leads to effective stress transfer through the ANF network by reducing the stress localization at the interface between fiber filler and matrix.

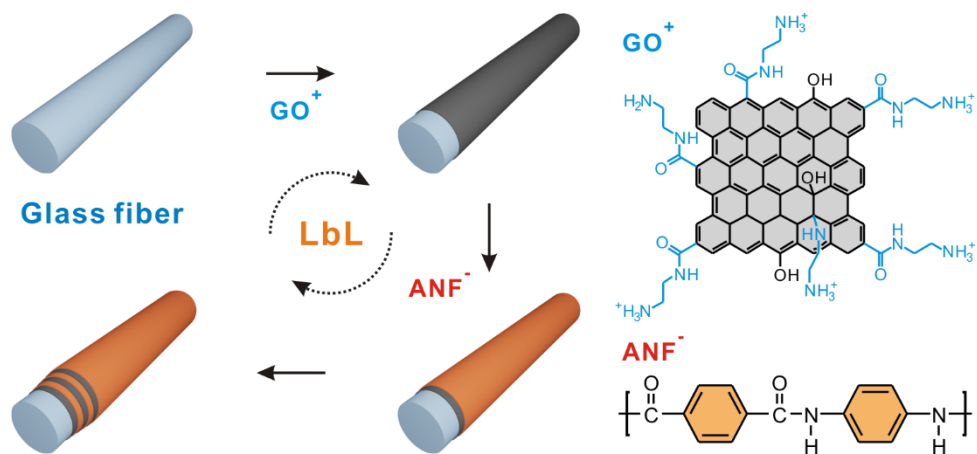


Figure 1. Schematic of the preparation of a positively charged graphene oxide (GO) and negatively charged aramid nanofiber (ANF) multilayer coating on a glass fiber via nanoscale blending layer-by-layer (LbL) assembly.

We present herein a simple, alternative approach to control the interfacial interaction of glass fiber with an epoxy matrix by coating a glass fiber with GO and ANF using a layer-by-layer (LbL) assembly (Figure 1). As a true nanoscale blending method, LbL assembly offers unique opportunities to prepare multilayer thin films of GO and ANF, with precise nanometer scale control over the thickness (i.e., the number of graphene sheets) and the structure, on solid surfaces.^{57–62} There have been a number of approaches, including our own, to combine the unique properties of graphene nanosheets with the versatility of LbL assembly for electronic devices, energy storage, gas sensors, and gas barriers.^{63–66} By taking advantage of LbL assembly, we also explored different combinations and sequences of layering in order to determine the impact of the architecture of coating layers on the mechanical properties of the composite. Specifically, we hypothesize that the surface functional groups present on the GO, such as epoxy groups, plays an important role of potential reactive anchoring sites within the epoxy matrix. The results showed that the integration of both GO and ANF significantly improved the interfacial adhesion and mechanical properties of the composites and, most interestingly, these properties were highly tunable depending on the number and sequence of layers, as well as the composition of the multilayers at the interface of the glass fiber filler and matrix.

II. Experimental method & materials

2.1. Synthesis of positively charged graphene oxide (GO)

Graphite oxide was synthesized by the modified Hummer's method,^{57,67} and then exfoliated under ultrasonication to yield a brown dispersion of GO in water. The resulting GO was negatively charged owing to the presence of chemical functional groups, such as carboxylic acids and alcohol groups. The negatively charged GO was transformed into positively charged GO by *N*-ethyl-*N'*-(3-dimethyl aminopropyl) carbodiimide methiodide (EDC) chemistry. Specifically, positively charged GO was synthesized by mixing 1.88 g of EDC (Sigma Aldrich) and 10 mL of ethylenediamine (99%, Sigma Aldrich) in 100 mL of negatively charged GO suspension (0.5 mg/mL) and stirring for 12 h. The resulting suspension was dialyzed (MWCO 12000-14000, Spectra/Por) for 7 days to remove any residues and byproducts. Prior to LbL deposition, the pH of positively charged GO suspension was adjusted to 3 with the addition of 1.0 M HCl.

2.2 Synthesis of aramid nanofiber (ANF)

ANF suspension was prepared from bulk Kevlar thread (Dupont) in dimethyl sulfoxide (DMSO) using potassium hydroxide (KOH), as previously reported by Kotov and co-workers.⁵⁶ Briefly, 0.04 g of Kevlar thread and 0.3 g of KOH were added to 100 mL of DMSO. The suspension was magnetically stirred for 1 week at room temperature, yielding a dark red ANF suspension in DMSO.

2.3. Surface modification of glass fibers by LbL assembly

The glass substrate used in the model system were cleaned using piranha solution (7:3 H₂SO₄/H₂O₂) for 1 h to remove any organic contamination. The cleaned glass substrates were treated by O₂-plasma to introduce a negatively charged surface. The substrate was first dipped in a positively charged GO solution (0.50 mg/mL) at pH 3 for 10 min. It was then rinsed in fresh deionized (DI) water for 1 min twice and then in DMSO for 2 min to remove loosely bound GO. Subsequently, the substrate was dipped in a negatively charged ANF suspension in DMSO for 10 min, and washed with DMSO twice for 1 min each and DI water for 2 min, which afforded a one-bilayer film of (GO/ANF)₁. In the case of (GO/PSS)₁, the substrate was first dipped in a positively charged GO solution for 10 min, then in DI water for 1 min twice, and finally, in 0.01 M NaCl for 2 min. Subsequently, the substrate was dipped in 1 wt% PSS solution (Poly(sodium 4-styrenesulfonate), *M_w* ~70,000, Sigma-Aldrich) in 0.10 M NaCl for 10 min, after which it was washed with fresh DI water for 1 min three times each. For (PDAC/ANF)₁, the substrate was first dipped in 1 wt% PDAC solution (Poly(diallyl dimethylammonium chloride), *M_w* <100,000, Sigma-Aldrich), then in DI water for 1 min twice, and, finally, in DMSO for 2 min. Subsequently, the substrate was dipped in ANF suspension for 10 min, and washed with DMSO twice for 1 min and DI water for 2 min. The above procedures were repeated to obtain the desired number of multilayers. Before surface modification of the glass fibers by LbL assembly, the glass fibers were treated by O₂-plasma for 30 s for them to obtain a negatively charged surface. Afterward, all other films were coated onto the glass fibers in a manner identical to that of the model system.

2.4. Sample preparation for microbond test

To measure the interfacial shear strength (IFSS) between the surface-modified glass fibers and the epoxy resin, microbond tests were carried out for single fibers having a micro-droplet of epoxy resin.⁶⁸ Testing fibers (35 mm in length) were vertically glued to a rectangular paper frame with outer and inner dimensions of 10 × 35 mm and 4 × 20 mm (width × length), respectively. A resin system was prepared by mixing a diglycidyl ether of bisphenol-A type epoxy resin (YD128, Kukdo Chemicals) with an anhydride curing agent (KBH1089, Kukdo Chemicals) in a weight ratio of 10:9. Using the tip of a single glass fiber, a micro-droplet of the prepared resin was applied to the center of the testing fiber, and then cured at 120 °C for 2 h.

2.5. Characterizations

Transmission electron microscopy (TEM) characterization of the ANF solution was performed using a JEOL-2100 with an accelerating voltage of 200kV, and the morphology of positively charged GO was investigated using tapping-mode atomic force microscopy (AFM, Nanoscope V, Veeco). The absorbance of the GO/ANF film was characterized by using UV-Vis spectroscopy (VARIAN, Cary 5000). The surface morphology of the modified glass fibers was characterized using scanning electron

microscopy (SEM, Hitachi, S-4800). The surface free energy (SFE) was characterized using a single fiber tensiometer (K100SF, Krüss). The microbond test for measuring IFSS was performed using a dynamic mechanical analysis (DMA) machine (Q800, TA Instruments) with a film tension grip, and the sizes of the droplet were measured by an optical microscope (LV100POL, Nikon).

III. Results & discussion

Initially, GO suspensions were prepared according to the modified Hummers method with pure graphite followed by exfoliation under ultrasonication. The as-prepared suspension of GO mainly comprises single-layer graphene nanosheets having a thickness of approximately 0.70 nm with lateral dimensions of 0.70–2.0 μm , as determined by AFM (Figure 2a). The amine functional groups were introduced on the surface of the GO through the EDC-mediated reaction between carboxylic acids (and/or epoxides) and excess ethylenediamine ($\text{NH}_2\text{CH}_2\text{CH}_2\text{NH}_2$) to afford a positively charged GO suspension, as reported previously.^{60,63,69} The as-prepared GO suspensions exhibited fairly good colloidal stability with a zeta-potential value of 38.3 mV owing to the presence of charged surface amine groups ($-\text{NH}_3^+$).

Separately, a stable dispersion of highly uniform ANFs was obtained through dissolution of commercial Kevlar fabric with KOH in DMSO based on the protocol reported by Kotov and co-workers. The diameter of the ANF was approximately 20 nm and its length was in the range of 5–10 μm , as determined from a collection of the TEM images. In addition, the abundant surface functional groups afforded the negatively charged ANF with a zeta-potential of -18.8 mV, ensuring the prerequisites for the LbL assembly with positively charged GO based on the electrostatic interactions.

With these two stable suspensions of positively charged GO and negatively charged ANFs, we fabricated multilayer films of $(\text{GO}/\text{ANF})_n$ by alternative dip-coating onto quartz slides as a model system to afford multilayers in an architecture of substrate/ $(\text{GO}/\text{ANF})_n$ (n = number of bilayers; typically, n = 2–10). The successful growth of $(\text{GO}/\text{ANF})_n$ multilayers was observed from a gradual increase of the UV/vis absorbance spectra with increasing number of bilayers that shows a characteristic absorbance of GO and the ANF within the multilayer film at 222 nm and 330 nm, respectively (Figure 3). The linear fitting of the absorbance value at 330 nm with respect to the number of bilayers clearly demonstrates well-controlled uniform assembly of the $(\text{GO}/\text{ANF})_n$ multilayers.

In LbL assembly, the internal structures of multilayers can be precisely tuned with a judicious choice of materials. We have exploited this principle to create another set of multilayers. First, to isolate the effect of modification from each other, we constructed only GO and ANF multilayers with conventional polyelectrolytes in a configuration of glass fiber/ $(\text{GO}/\text{PSS})_n$ and

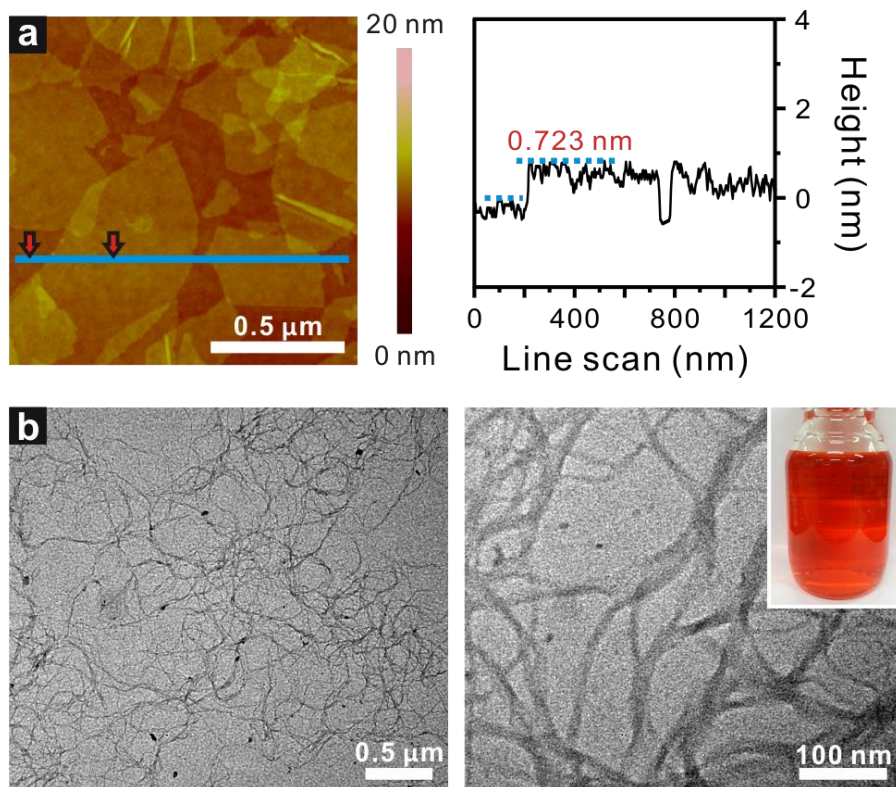


Figure 2. (a) AFM image and height profile of graphene oxide (GO) and (b) TEM images of the aramid nanofiber (ANF) derived from Kevlar threads. The inset in part b shows the suspension of the ANF in dimethyl sulfoxide.

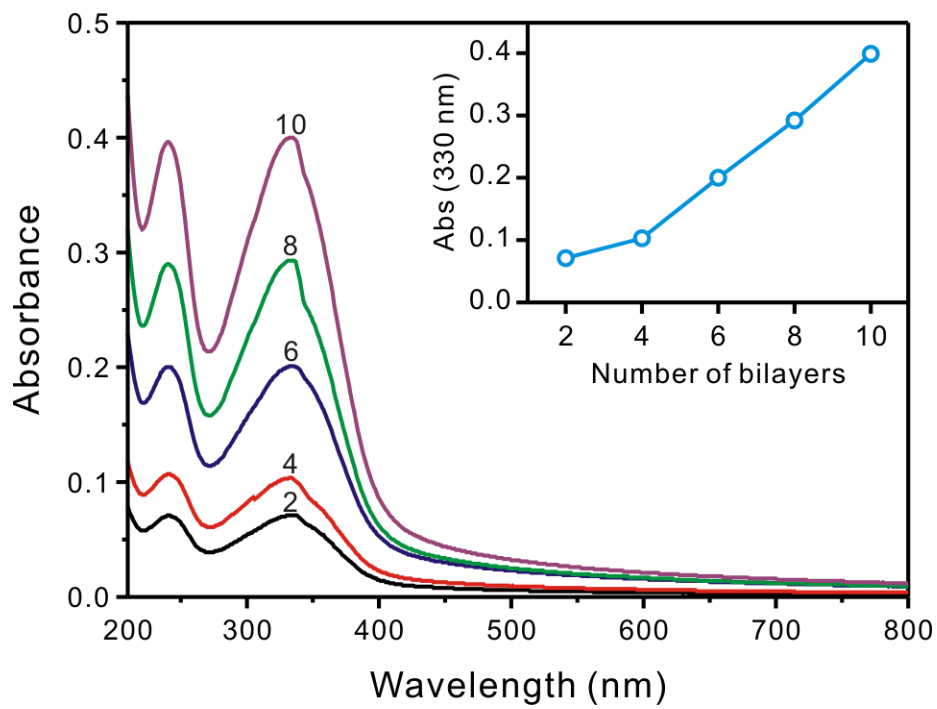


Figure 3. UV/vis spectra of GO/ANF multilayer films as a function of the number of bilayers. The inset indicates the absorbance at 330 nm depending on the number of bilayers.

glass fiber/(PDAC/ANF)_n, respectively (herein, PSS is poly(styrene sulfonate) and PDAC is poly(dimethyldiallylammonium chloride)). Second, we fabricated the two different sets of multilayers onto the glass fiber in different sequences of layering, such as glass fiber/(GO/ANF)_n and glass fiber/(PDAC/ANF)_n/(GO/PSS)_n. The architecture and notation of the multilayer-coated glass fibers are summarized in Table 1. As highlighted in the introduction, we hypothesized that the surface functional groups present on the GO and the superior mechanical property of the ANF are envisioned to provide additional opportunities to drastically improve the fiber-matrix stress transfer of glass fiber with epoxy resin for enhanced mechanical properties.

The surface morphology of the multilayers deposited on the glass fiber was examined with SEM as shown in Figure 4. It is observed that the multilayers are formed on the surface of the glass fibers with no severe agglomeration, owing to LbL assembly, which could offer fine control in the multilayer stacking. Figure 4a shows the uniformly coated morphology of GO₁₀, where GO and the polyelectrolyte are stacked. The glass fibers were well covered by the multilayer with GO in a characteristic wrinkled surface structure, demonstrating highly flexible two-dimensional GO sheets. Likewise, ANF₁₀ was successfully deposited onto the surface of the glass fibers by LbL assembly. The enlarged image in Figure 4b shows the one-dimensional fibril microstructure of the ANF in the multilayer.

For the LbL assembly between GO and ANF, Figure 4c and 4d show the surface morphology of (GO/ANF)₁₀ without the conventional polyelectrolyte and ANF₅/GO₅ with the polyelectrolyte, respectively. The multilayer of (GO/ANF)₁₀ provided relatively low coverage of the whole surface, in particular, some sections appear to be separated from the glass fiber. On the other hand, the coated structure of ANF₅/GO₅ is similar in morphology to that of GO₁₀ that is assembled with polyelectrolyte layers. This suggests that the polyelectrolyte layers can function as a support to immobilize the micro-sized GO and ANF during the LbL assembly, resulting in a brick-and-mortar structure.⁷⁰ These results show that the LbL assembly makes it possible to assemble the two-dimensional GO and one-dimensional ANF within a single multilayer structure even onto the curved surface of a glass fiber. Additional cross-sectional SEM images supported the successful coating of thin layers of GO and ANF on the surface of glass fiber (Figure S2 in Supporting Information). We also confirmed that the assembly condition did not damage the original morphology of the glass fiber during the surface modification process.

To evaluate the surface properties of multilayer-coated glass fibers, the SFE of each modified glass fiber was monitored based on the Owens–Wendt method,⁷¹ as shown in Figure 5. Specifically, the SFE of the modified glass fiber was calculated by measuring the contact angle with distilled water (H₂O) and diiodomethane (CH₂I₂) to account for the contribution of the polar and dispersive parts of the SFE, respectively. While GO₁₀ had only a moderate increase of 10.4% in the dispersive part of the SFE, it showed a significant increase of 48.5% in the polar part of the SFE compared with the bare

Table 1. Configuration of the multilayer-coated glass fibers.

entry	architecture	notation
1	glass fiber/(GO/PSS) _n	GO _n
2	glass fiber/(PDAC/ANF) _n	ANF _n
3	glass fiber/(GO/ANF) _n	(GO/ANF) _n
4	glass fiber/(PDAC/ANF) _n /(GO/PSS) _n	ANF _n /GO _n

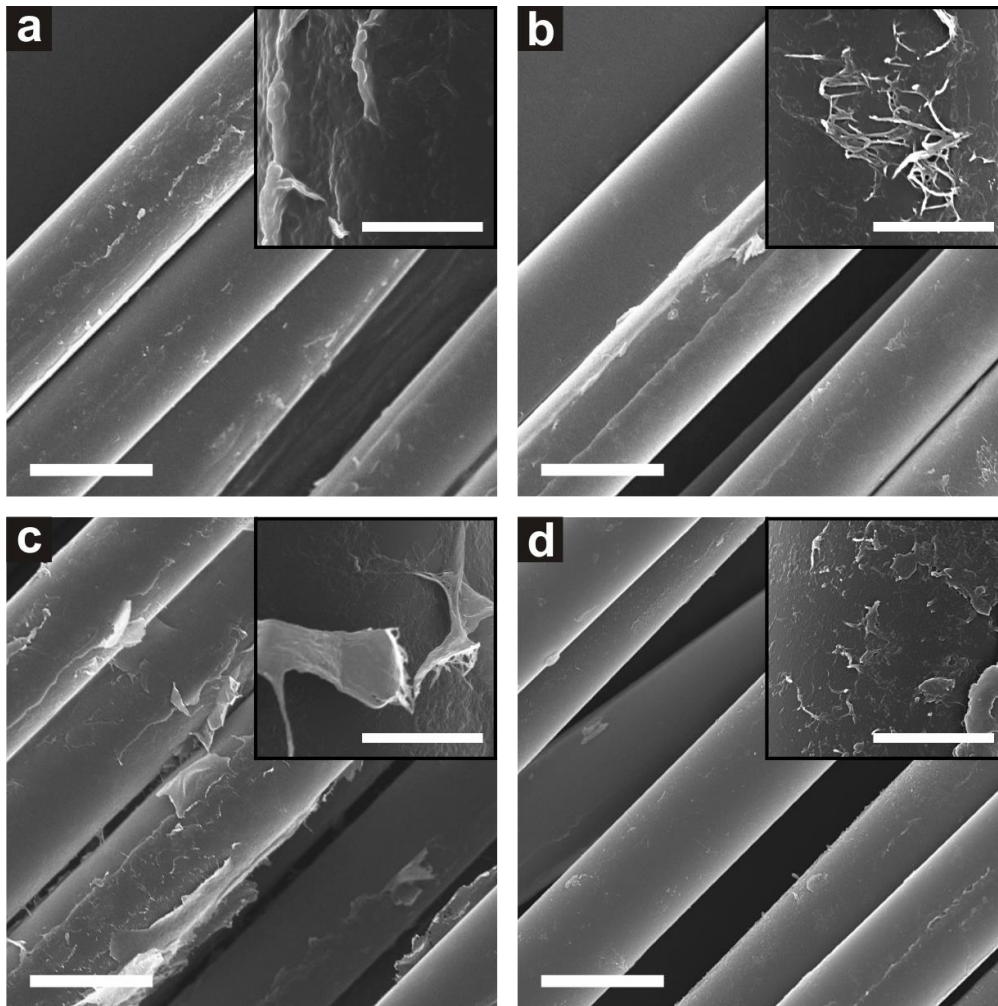


Figure 4. SEM images of multilayer-coated glass fibers of (a) GO_{10} , (b) ANF_{10} , (c) $(GO/ANF)_{10}$, and (d) ANF_5/GO_5 . The inset shows an enlarged view of each glass fiber. The scale bars are 20 μm (4 μm in the insets).

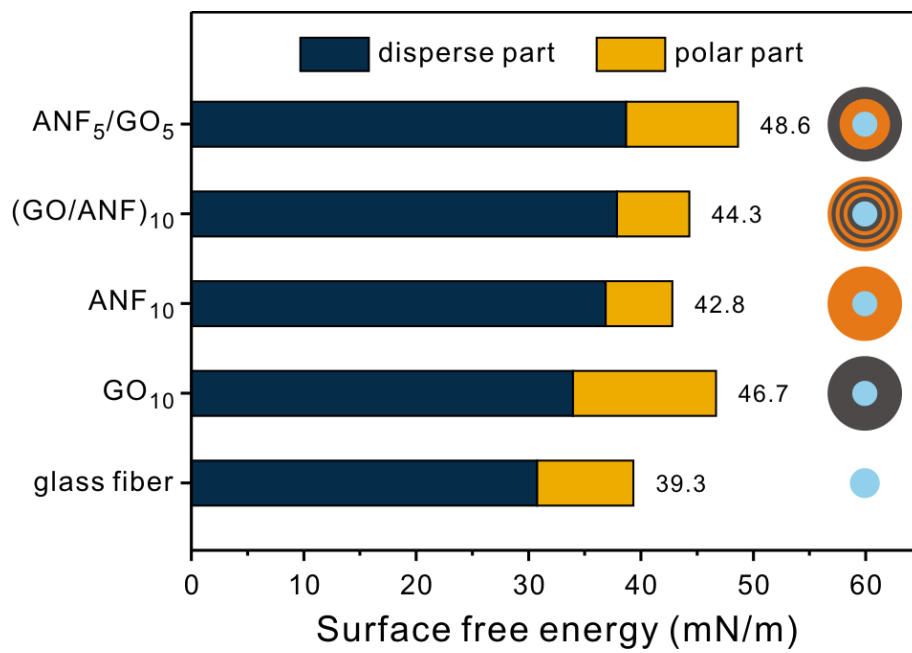


Figure 5. Surface free energy of the multilayer-coated glass fibers with different assembly and their corresponding schematics representing the glass fiber (sky-blue), GO layer (gray), and ANF layer (orange).

glass fiber whose SFE was 8.6 and 30.8 mN/m for the polar and dispersive parts, respectively. This suggests that the abundant oxygen functional groups and amine group in GO could contribute to the enhancement of the polar part of the SFE. In the case of ANF₁₀, the dispersive part of the SFE increased by 19.8% compared with that of bare glass fiber, owing to the aromatic segment and amide groups within the structure of the ANF, while the polar part decreased by 30.6%. Thus, it is considered that the ANF modification causes an increase in the dispersive part of the SFE, which is not the case for the polar part. Furthermore, the effect of the number of multilayers (i.e., multilayer thickness) was examined by utilizing the advantage of LbL assembly. Interestingly, the total SFE did not noticeably increase even in GO₃₀ and ANF₃₀ for the configuration of 30 bilayers (Figure S1 in Supporting Information), indicating that the LbL assembly with 10 bilayers is sufficient for the surface modification of a glass fiber.

In the hybrid architecture of GO and ANF hybrid multilayers, both (GO/ANF)₁₀ and ANF₅/GO₅ showed increased SFE, particularly for the dispersive part. The greatest increase in SFE was observed for the ANF₅/GO₅ configuration, where the polar and dispersive parts of the SFE were 9.93 and 38.69 mN/m, respectively. The dispersive part of the SFE of ANF₅/GO₅ exhibited a significant increase of 25.8%, whereas the polar part decreased slightly compared with that of GO₁₀, owing to the introduction of the ANF. Thus, it is obvious that the integration of GO and ANFs with LbL assembly could simultaneously improve both the polar and dispersive parts of the SFE. However, the SFE of (GO/ANF)₁₀ remained almost the same as that of ANF₁₀ in spite of the presence of GO layers. This suggests that the polyelectrolyte in the multilayers may play a role in the increased SFE of a glass fiber, especially for the polar part. This difference originates from the unique feature of LbL assembly that provides fine control over the architecture with a simple change in the assembly sequence.

The interfacial adhesion property between the multilayer-coated glass fibers and epoxy matrix was evaluated based on IFSS using a microbond test (Figure 6a and 6b). The IFSS of each specimen was calculated by the equation

$$\tau_{\text{IFSS}} = \frac{F_d}{\pi D_f L_e}$$

Where F_d is the pullout force at debonding, D_f is the diameter of glass fiber, and L_e is the embedded length of glass fiber in epoxy matrix. In Figure 6c, the surface area of the glass fiber through the epoxy matrix and the pullout force at the debonding correlate well with a linear fit. The IFSS of all of the multilayer-coated glass fibers increased in comparison with that of a bare glass fiber, which is 20.74 MPa, in agreement with a previous report.^{72,73} These enhancements in the IFSS correlate with those in the SFE of each configuration of the glass fiber, as summarized in Table 2.

As expected, ANF₅/GO₅ exhibits the greatest IFSS (39.2% greater than that of bare glass) among

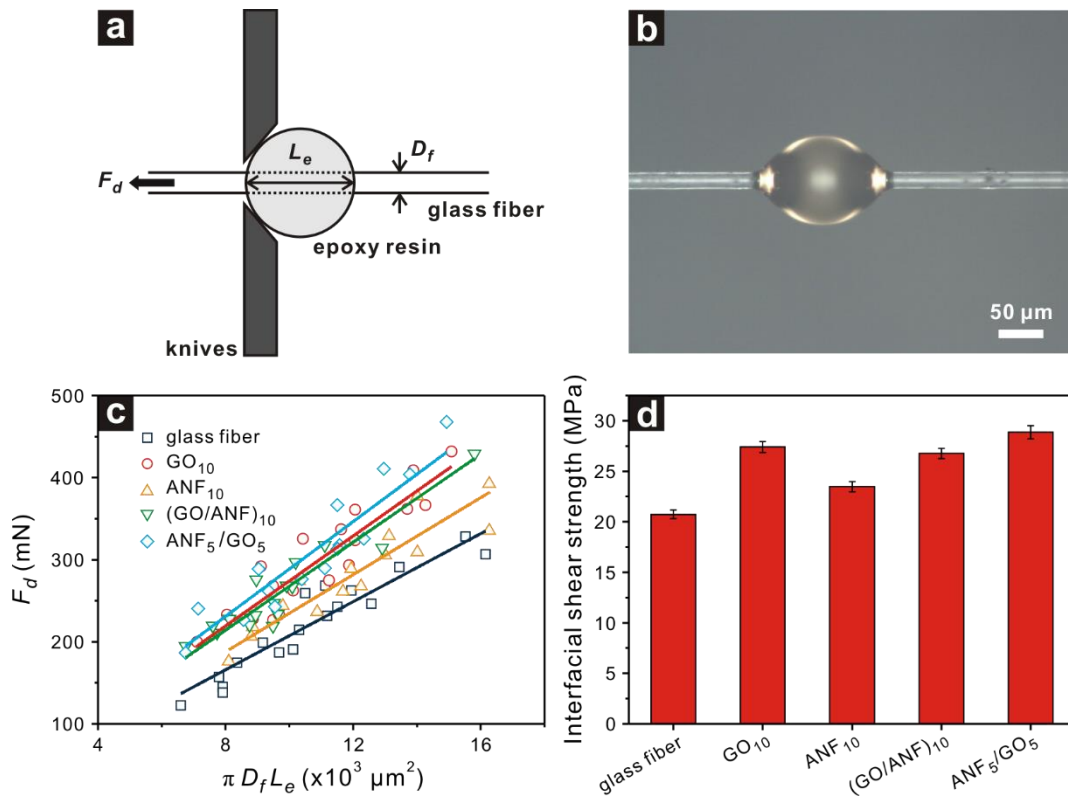


Figure 6. (a) Schematic of the microbond test for interfacial shear strength (IFSS). Epoxy resin is held in place with knives and measurement is carried out by pulling out a glass fiber. (b) Optical microscope image of the micro-droplet of epoxy resin on the glass fiber. (c) Pull-out force distribution depending on the immersion area within the epoxy matrix, and (d) Derived IFSS of the multilayer-coated glass fibers.

Table 2. Measured surface free energy (SFE) and interfacial shear strength (IFSS).

sample	SFE (mN/m)			IFSS (MPa)
	polar part	dispersive part	total	
glass fiber	8.57	30.76	39.33	20.74
GO ₁₀	12.73	33.96	46.68	27.40
ANF ₁₀	5.95	36.85	42.80	23.47
(GO/ANF) ₁₀	6.45	37.86	44.31	26.77
ANF ₅ /GO ₅	9.93	38.69	48.63	28.86

all the samples tested, which is consistent with the total SFE value obtained in Figure 5. Surface modification with polar functional groups leads to the enhancement of the polar part of the SFE, which can improve the degree of wetting. In addition, these functional groups participate in the curing reaction by forming covalent bonds.^{73,74} Thus, the introduction of GO including abundant oxygen and amine functional groups could provide a reactive anchoring site for the epoxy matrix as well as compatibility with the epoxy matrix on the glass fiber. The introduction of the ANF significantly enhances the dispersive part of the SFE by improving the overall IFSS. Considering the SFE of (GO/ANF)₁₀, it is evident that the IFSS of (GO/ANF)₁₀ is lower than that of ANF₅/GO₅, though the number of GO and ANF layers in (GO/ANF)₁₀ is twice that in ANF₅/GO₅. This shows that the interfacial properties between the glass fiber and epoxy matrix are highly tunable depending on the configuration of GO and ANF multilayer coating, even under identical composition of multilayers.

IV. Conclusion

In conclusion, we successfully assembled GO and ANF multilayers onto a glass fiber with facile architecture control by LbL assembly in order to enhance the interfacial properties between the glass fiber and epoxy matrix. The LbL assembly facilitated the development of the assembly of multi-dimensional nanomaterials without significant phase aggregation and controlled architecture among the layers. The configuration of the GO and ANF layers had a significant influence on the surface properties of the glass fiber. In particular, the increase of polar and dispersive parts of the SFE of multilayer-coated glass fibers was mainly attributed to the GO and ANF layers, respectively. The enhancement of the IFSS between the glass fiber and epoxy matrix was consistent with that of the total SFE of the multilayer-coated glass fiber, which depends on the configuration of the GO and ANF multilayers. Therefore, the integrated architecture of GO and ANF hybrid multilayers with fine controlled LbL assembly is expected to improve the interfacial properties of the diverse nanocomposites as well as those of the glass fiber/epoxy composites. Furthermore, it is considered that the LbL assembly could offer an opportunity to optimize the interfacial properties of nanocomposites with identical composition of coating materials.

References

1. Liu, J.; Wickramaratne, N. P.; Qiao, S. Z.; Jaroniec, M. *Nat. Mater.* **2015**, *14*, 763–774.
2. Deshmukh, A. A.; Mhlanga, S. D.; Coville, N. J. *Mater. Sci. Eng. R Reports* **2010**, *70*, 1–28.
3. Nieto-Márquez, A.; Romero, R.; Romero, A.; Valverde, J. L. *J. Mater. Chem.* **2011**, *21*, 1664–1672.
4. Kim, T.-W.; Chung, P.-W.; Slowing, I. I.; Tsunoda, M.; Yeung, E. S.; Lin, V. S.-Y. *Nano Lett.* **2008**, *8*, 3724–3727.
5. Liang, H.-W.; Zhuang, X.; Brüller, S.; Feng, X.; Müllen, K. *Nat. Commun.* **2014**, *5*, 4973.
6. Sun, Z.; Liu, Y.; Li, B.; Wei, J.; Wang, M.; Yue, Q.; Deng, Y.; Kaliaguine, S.; Zhao, D. *ACS Nano* **2013**, *7*, 8706–8714.
7. White, R. J.; Tauer, K.; Antonietti, M.; Titirici, M.-M. *J. Am. Chem. Soc.* **2010**, *132*, 17360–17363.
8. Liu, R.; Mahurin, S. M.; Li, C.; Unocic, R. R.; Idrobo, J. C.; Gao, H.; Pennycook, S. J.; Dai, S. *Angew. Chem., Int. Ed.* **2011**, *50*, 6799–6802.
9. Fuertes, A. B.; Valle-Vigón, P.; Sevilla, M. *Chem. Commun.* **2012**, *48*, 6124–6126.
10. Zhang, K.; Zhao, Q.; Tao, Z.; Chen, J. *Nano Res.* **2013**, *6*, 38–46.
11. Li, N.; Zhang, Q.; Liu, J.; Joo, J.; Lee, A.; Gan, Y.; Yin, Y. *Chem. Commun.* **2013**, *49*, 5135–5137.
12. Feng, S.; Li, W.; Shi, Q.; Li, Y.; Chen, J.; Ling, Y.; Asiri, A. M.; Zhao, D. *Chem. Commun.* **2014**, *50*, 329–331.
13. Qiao, Z.-A.; Guo, B.; Binder, A. J.; Chen, J.; Veith, G. M.; Dai, S. *Nano Lett.* **2013**, *13*, 207–212.
14. Han, J.; Xu, G.; Ding, B.; Pan, J.; Dou, H.; MacFarlane, D. R. *J. Mater. Chem. A* **2014**, *2*, 5352–5357.
15. Liang, C.; Hong, K.; Guiochon, G. A.; Mays, J. W.; Dai, S. *Angew. Chem., Int. Ed.* **2004**, *43*, 5785–5789.
16. Liang, C.; Li, Z.; Dai, S. *Angew. Chem., Int. Ed.* **2008**, *47*, 3696–3717.
17. Meng, Y.; Gu, D.; Zhang, F.; Shi, Y.; Yang, H.; Li, Z.; Yu, C.; Tu, B.; Zhao, D. *Angew. Chem., Int. Ed.* **2005**, *44*, 7053–7059.
18. Tanaka, S.; Nishiyama, N.; Egashira, Y.; Ueyama, K. *Chem. Commun.* **2005**, No. 16, 2125–2127.
19. Wan, Y.; Shi, Y.; Zhao, D. *Chem. Mater.* **2008**, *20*, 932–945.
20. Fang, Y.; Gu, D.; Zou, Y.; Wu, Z.; Li, F.; Che, R.; Deng, Y.; Tu, B.; Zhao, D. *Angew. Chem., Int. Ed.* **2010**, *49*, 7987–7991.
21. Liu, J.; Yang, T.; Wang, D.-W.; Lu, G. Q.; Zhao, D.; Qiao, S. Z. *Nat. Commun.* **2013**, *4*, 2798.

22. Gu, D.; Bongard, H.; Deng, Y.; Feng, D.; Wu, Z.; Fang, Y.; Mao, J.; Tu, B.; Schüth, F.; Zhao, D. *Adv. Mater.* **2010**, *22*, 833–837.
23. Tang, J.; Liu, J.; Li, C.; Li, Y.; Tade, M. O.; Dai, S.; Yamauchi, Y. *Angew. Chem., Int. Ed.* **2015**, *54*, 588–593.
24. Yan, Y.; Zhang, F.; Meng, Y.; Tu, B.; Zhao, D. *Chem. Commun.* **2007**, No. 27, 2867–2869.
25. Wu, Z.; Wu, W. D.; Liu, W.; Selomulya, C.; Chen, X. D.; Zhao, D. *Angew. Chem., Int. Ed.* **2013**, *52*, 13764–13768.
26. Xu, F.; Tang, Z.; Huang, S.; Chen, L.; Liang, Y.; Mai, W.; Zhong, H.; Fu, R.; Wu, D. *Nat. Commun.* **2015**, *6*, 7221.
27. Yang, Z.-C.; Zhang, Y.; Kong, J.-H.; Wong, S. Y.; Li, X.; Wang, J. *Chem. Mater.* **2013**, *25*, 704–710.
28. Sun, X.; Li, Y. *Angew. Chem., Int. Ed.* **2004**, *43*, 597–601.
29. Hu, B.; Wang, K.; Wu, L.; Yu, S.-H.; Antonietti, M.; Titirici, M.-M. *Adv. Mater.* **2010**, *22*, 813–828.
30. Shin, Y.; Wang, L.-Q.; Bae, I.-T.; Arey, B. W.; Exarhos, G. J. *J. Phys. Chem. C* **2008**, *112*, 14236–14240.
31. Scholz, S.; Leech, P. J.; Englert, B. C.; Sommer, W.; Weck, M.; Bunz, U. H. F. *Adv. Mater.* **2005**, *17*, 1052–1056.
32. Agrawal, M.; Gupta, S.; Stamm, M. *J. Mater. Chem.* **2011**, *21*, 615–627.
33. Ouyang, Y.; Shi, H.; Fu, R.; Wu, D. *Sci. Rep.* **2013**, *3*.
34. Liu, J.; Qiao, S. Z.; Liu, H.; Chen, J.; Orpe, A.; Zhao, D.; Lu, G. Q. *Angew. Chem., Int. Ed.* **2011**, *50*, 5947–5951.
35. Zhao, J.; Niu, W.; Zhang, L.; Cai, H.; Han, M.; Yuan, Y.; Majeed, S.; Anjum, S.; Xu, G. *Macromolecules* **2013**, *46*, 140–145.
36. Zhou, J.; Lian, J.; Hou, L.; Zhang, J.; Gou, H.; Xia, M.; Zhao, Y.; Strobel, T. A.; Tao, L.; Gao, F. *Nat. Commun.* **2015**, *6*, 6803.
37. Wu, J.; Rui, X.; Long, G.; Chen, W.; Yan, Q.; Zhang, Q. *Angew. Chem., Int. Ed.* **2015**, *54*, 7354–7358.
38. Shock, E. L. *Geochim. Cosmochim. Acta* **1993**, *57*, 3341–3349.
39. Benmokrane, B.; Wang, P.; Ton-That, T. M.; Rahman, H.; Robert, J. F. *J. Compos. Constr.* **2002**, *6*, 143–153.
40. Mallick, P. K. *Fiber-Reinforced Composites: Materials, Manufacturing, and Design*; Marcel Dekker: New York, 1993.
41. De Rosa, I. M.; Sarasini, F.; Sarto, M. S.; Tamburrano, A. *IEEE Trans. Electromagn. Compat.* **2008**, *50*, 556–563.
42. George, J.; Sreekala, M. S.; Thomas, S. *Polym. Eng. Sci.* **2001**, *41*, 1471–1485.

43. Thostenson, E. T.; Li, W. Z.; Wang, D. Z.; Ren, Z. F.; Chou, T. W. *J. Appl. Phys.* **2002**, *91*, 6034–6037.
44. Novoselov, K. S.; Geim, A. K.; Morozov, S. V.; Jiang, D.; Zhang, Y.; Dubonos, S. V.; Grigorieva, I. V.; Firsov, A. A. *Science* **2004**, *306*, 666–669.
45. Stankovich, S.; Dikin, D. A.; Dommett, G. H. B.; Kohlhaas, K. M.; Zimney, E. J.; Stach, E. A.; Piner, R. D.; Nguyen, S. T.; Ruoff, R. S. *Nature* **2006**, *442*, 282–286.
46. Schedin, F.; Geim, A. K.; Morozov, S. V.; Hill, E. W.; Blake, P.; Katsnelson, M. I.; Novoselov, K. S. *Nat. Mater.* **2007**, *6*, 652–655.
47. Dreyer, D. R.; Park, S.; Bielawski, C. W.; Ruoff, R. S. *Chem. Soc. Rev.* **2010**, *39*, 228–240.
48. Park, S.; Dikin, D. A.; Nguyen, S. T.; Ruoff, R. S. *J. Phys. Chem. C* **2009**, *113*, 15801–15804.
49. Kim, H.; Miura, Y.; MacOsko, C. W. *Chem. Mater.* **2010**, *22*, 3441–3450.
50. Steurer, P.; Wissert, R.; Thomann, R.; Mülhaupt, R. *Macromol. Rapid Commun.* **2009**, *30*, 316–327.
51. Fang, M.; Wang, K.; Lu, H.; Yang, Y.; Nutt, S. *J. Mater. Chem.* **2009**, *19*, 7098–7105.
52. Potts, J. R.; Dreyer, D. R.; Bielawski, C. W.; Ruoff, R. S. *Polymer* **2011**, *52*, 5–25.
53. Tanner, D.; Fitzgerald, J. A.; Phillips, B. R. *Angew. Chem., Int. Ed.* **1989**, *28*, 649–654.
54. Kitano, T.; Haghani, E.; Tanegashima, T.; Saha, P. *Polym. Compos.* **2000**, *21*, 493–505.
55. Saikrasun, S.; Amornsakchai, T.; Sirisinha, C.; Meesiri, W.; Bualek-Limcharoen, S. *Polymer* **1999**, *40*, 6437–6442.
56. Yang, M.; Cao, K.; Sui, L.; Qi, Y.; Zhu, J.; Waas, A.; Arruda, E. M.; Kieffer, J.; Thouless, M. D.; Kotov, N. A. *ACS Nano* **2011**, *5*, 6945–6954.
57. Kovtyukhova, N. I. *Chem. Mater.* **1999**, *11*, 771–778.
58. Lvov, Y.; Ariga, K.; Ichinose, I.; Kunitake, T. *J. Am. Chem. Soc.* **1995**, *117*, 6117–6123.
59. Shen, J.; Hu, Y.; Li, C.; Qin, C.; Shi, M.; Ye, M. *Langmuir* **2009**, *25*, 6122–6128.
60. Hong, J.; Han, J. Y.; Yoon, H.; Joo, P.; Lee, T.; Seo, E.; Char, K.; Kim, B.-S. *Nanoscale* **2011**, *3*, 4515–4531.
61. Yan, Y.; Björnalm, M.; Caruso, F. *Chem. Mater.* **2014**, *26*, 452–460.
62. Ariga, K.; Yamauchi, Y.; Rydzek, G.; Ji, Q.; Yonamine, Y.; Kevin, C.-W.; Hill, J. P. *Chem. Lett.* **2014**, *43*, 36–68.
63. Hwang, H.; Joo, P.; Kang, M. S.; Ahn, G.; Han, J. T.; Kim, B.-S.; Cho, J. H. *ACS Nano* **2012**, *6*, 2432–2440.
64. Yu, D.; Dai, L. *J. Phys. Chem. Lett.* **2010**, *1*, 467–470.
65. Ji, Q.; Honma, I.; Paek, S.-M.; Akada, M.; Hill, J. P.; Vinu, A.; Ariga, K. *Angew. Chem., Int. Ed.* **2010**, *49*, 9737–9739.
66. Yang, Y.-H.; Bolling, L.; Priolo, M. A.; Grunlan, J. C. *Adv. Mater.* **2013**, *25*, 503–508.
67. Hummers Jr., W. S.; Offeman, R. E. *J. Am. Chem. Soc.* **1958**, *80*, 1339.

68. Miller, B.; Muri, P.; Rebenfeld, L. *Compos. Sci. Technol.* **1987**, *28*, 17–32.
69. Lee, D. W.; Hong, T.-K.; Kang, D.; Lee, J.; Heo, M.; Kim, J. Y.; Kim, B.-S.; Shin, H. S. *J. Mater. Chem.* **2011**, *21*, 3438–3442.
70. Michel, M.; Arntz, Y.; Fleith, G.; Toquant, J.; Haikel, Y.; Voegel, J.-C.; Schaaf, P.; Ball, V. *Langmuir* **2006**, *22*, 2358–2364.
71. Owens, D. K.; Wendt, R. C. *J. Appl. Polym. Sci.* **1969**, *13*, 1741–1747.
72. Netravali, A. N.; Stone, D.; Ruoff, S.; Topoleski, L. T. T. *Compos. Sci. Technol.* **1989**, *34*, 289–303.
73. Moon, C. K.; Lee, J.-O.; Cho, H. H.; Kim, K. S. *J. Appl. Polym. Sci.* **1992**, *45*, 443–450.
74. Zhu, J.; Wei, S.; Ryu, J.; Budhathoki, M.; Liang, G.; Guo, Z. *J. Mater. Chem.* **2010**, *20*, 4937–4948.

* PART 2 is reproduced in part with permission from ACS Appl. Mater. Interfaces 2015, 7, 3329–3334.

Copyright 2015 American Chemical Society.

감사의 글

학부생 2학년부터 지내왔던 KBS group 에서의 연구생활이 얼마 남지 않은 것을 이제야 실감하면서 감사의 글을 올립니다. 4년여 간의 시간 동안 많은 것을 가르쳐 주신 김병수 지도교수님께 감사하고 존경한다는 말씀을 먼저 드리고 싶습니다. 연구실에서 학술대회나 논문 게재 같은 귀중한 경험들을 할 수 있는 기회를 주셔서 진심으로 감사 드립니다. 또한 졸업 심사를 선뜻 맡아주신 권태혁 교수님, 정윤석 교수님께도 감사 드립니다.

연구실의 멤버들께도 고마움을 전합니다. 박사란 무엇인지 알게 해주시는 정윤경 박사님, 민사훈 박사님, 송수희 박사님께 먼저 감사의 말씀을 드립니다. 그리고 미국에서 열심히 연구하고 계신 큰형님 은용이 형, 처음 들어왔을 때부터 많은 것을 가르쳐주시는 태민이 형, 고민이 있을 때마다 조언과 따뜻한 말을 해주시는 유리 누나, 방장으로서 많은 일들에 고생하시는 응진이 형, 까칠한 듯 후배들을 챙겨주시는 민수 형, 동아리 생활부터 꽤 오래 얼굴을 봐온 이슬 누나께도 여러 가지로 감사했습니다. 밝지만 은근히 세심한 민주와 말이 잘 통하는 준희 형 두 명에게는 동기들이 있어서 실험실 생활에 많은 힘이 되었다는 말을 전하며, 새로이 입학하는 재은이, 영규, 해리 세 명에게는 갓 시작된 연구실 생활에서 많은 것들을 배워갈 수 있기를 바랍니다. 또 학교를 떠나서도 많은 도움을 주시는 기영이 형, 미국에서 박사 학위를 시작하시는 필재 형, 그리고 논문을 쓸 수 있게 큰 도움을 주신 은희 누나와 박수진 교수님 연구실 태수 형께도 감사하다는 말씀을 드려야 할 것 같습니다.

짧지 않은 울산 생활에서 언제나 돌아갈 곳이 되어준 가족들께도 감사를 드립니다. 평소 표현은 못했지만 존경하고 사랑하는 아버지와 어머니, 이 졸업논문을 보셨으면 너무나 자랑스러워 하셨을 할머니, 먼 곳에서 직장 생활하며 고생하는 우리 누나, 대학생 생활에 한창 바쁜 동생 연이, 힘들 때 제일 큰 힘이 되어주시는 작은 고모 그리고 다른 친척들께 자랑스러운 사람이 될 수 있도록 노력 하겠습니다.

마지막으로, 배울 것이 많은 때로는 형 같은 룸메이트 재건이, 늘 공부하느라 고생하는 덕규, 대학생의 자유를 즐기고 있는 태일이, 이제는 회사원 생활에 적응해가고 있는 창배, 바쁘지 연락이 뜸한 20년지기 친구 영세에게도 고맙습니다. 또 UNIST 생활에서 소중한 활력소였던 현악합주 동아리 CZARDAS, 학교 공식 오케스트라 UNISTRA 친구들, 그리고 두 단체의 지도 교수님이신 이종은 교수님께 같이 연주할 수 있어서 개인적으로 큰 기쁨이었다는 말을 드립니다.

무사히 석사 학위를 마칠 수 있도록 도와주신 모든 분들께 다시 한번 감사를 드리며 이 글을 마칩니다.